ACS Catalysis

pubs.acs.org/acscatalysis

Perspective

Progress and Opportunities in Photochemical Enzymology of Oxidoreductases

Brandon L. Greene*

Cite This: *ACS Catal.* 2021, 11, 14635−14650

Read Online

ACCESS | Metrics & More | Article Recommendations

ABSTRACT: The mechanistic enzymology of oxidoreductases has contributed to the development of therapeutics, biomimetic synthetic catalysts, and engineered enzymes with improved or emergent function. Acquiring the atomic detail of an oxidoreductase's mechanism is challenging, however, as the reaction coordinate is generally complex and the chemical steps of interest are often kinetically obscured. Recently, photosynthesis-inspired strategies have been applied to rapidly initiate oxidoreductase catalysis with light for mechanistic investigations, namely, the chemical potential jump (μ-jump) method and the design of artificially photosynthetic enzymes. While these methods are commonplace in (bio)-photocatalysis, they are less frequently leveraged to gain insight into the oxidoreductase function. When paired with the appropriate spectroscopic tools to follow the ensuing events, such rapid initiation strategies enable the observation of chemical steps on time scales inaccessible by conventional mixing techniques. This Perspective summarizes the contributions of rapid initiation strategies to the mechanistic understanding of hydrogenases and artificially photosynthetic ribonucleotide reductases. Opportunities in other oxidoreductases are discussed.

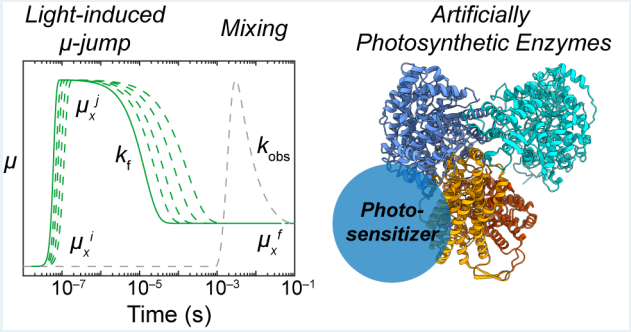

KEYWORDS: *Chemical potential jump, artificial photosynthetic enzymes, enzymology, oxidoreductase*

1. INTRODUCTION

Oxidoreductases are a class of enzymes that catalyze the reduction or oxidation of substrates and are central to cellular energy transduction, metabolism, regulation, and maintenance. Their biochemical functions have been targeted for therapeutic development, and several prescribed and over-the-counter drugs act on oxidoreductases including common nonsteroidal anti-inflammatory drugs,[1] statins,[2] and chemotherapeutics.[3−5] A number of oxidoreductases are also a source of inspiration to chemists interested in catalyst design,[6−8] facilitating attractive yet challenging reactions under mild conditions such as water oxidation (photosystem II), proton reduction (hydrogenases), nitrogen fixation (nitrogenases), CO_2 fixation (e.g., formate dehydrogenase), or selective C−H bond activation (e.g., cytochrome P450). Advances in protein engineering, informed by mechanistic insight, have also expanded substrate scope, product selectivity, and catalytic function on oxidoreductase scaffolds.[9−11] Whether an oxidoreductase is of interest as a therapeutic target, a catalyst blueprint, or an engineering platform, the molecular details of the native mechanism provide a chemical entry point to diverse applications and a window through which to understand Nature's catalytic design principles.

To establish the mechanism of any enzyme, kinetic analysis of reaction progression, reaction intermediates, and their interconversion is necessary. For oxidoreductases specifically, this may involve monitoring reaction progression after mixing of two or more solutions containing the enzyme, substrate, and oxidant or reductant. Intermediates along the complete reaction coordinate can be obscured in such a kinetic experiment in the steady state, where the observed rate is dictated by the rate-determining step(s) in a multistep catalytic cycle. The situation is acute in the oxidoreductases, where the time scales of diffusion-limited substrate or cofactor binding, the conformational search for a reactive enzyme−substrate complex, and product release often occur on distinctly slower time scales than the chemical steps, namely, electron transfer (ET) or proton-coupled electron transfer (PCET) and bond formation or rupture.[12−14] Rapid mixing by stopped- or continuous-flow can afford a glimpse into an enzyme's approach to the steady state, and thus chemical events that precede the rate-determining step, but mixing is limited in time resolution by fluid dynamics; homogeneous mixing is rarely achieved faster than 1−10 ms.

Received: October 1, 2021
Revised: October 28, 2021
Published: November 19, 2021

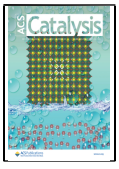

https://doi.org/10.1021/acscatal.1c04525
ACS Catal. 2021, 11, 14635−14650

How then might fast (>10^3 s^{-1}) chemical events in oxidoreductase catalysis be resolved for mechanistic investigation? The answer lies, in part, in adapting strategies from the photosystems of photosynthesis and synthetic photocatalysis, where light absorption initiates redox chemistry. While most oxidoreductases are not naturally photosynthetic, advances in photochemistry and protein engineering have been developed to rapidly initiate oxidoreductase catalysis with light, broadening the time scales accessible to kinetic investigations.

In this Perspective, two rapid photochemical initiation methods, the chemical potential jump (μ-jump) and the direct initiation of artificial photosynthetic enzymes, are presented. When rapid initiation methods are accompanied by spectroscopic techniques of sufficient molecular and temporal resolution, profound insight into the mechanism can be achieved with intimate detail. The number of oxidoreductases investigated by rapid photochemical initiation is, at present, modest, but it is hoped that the methods described below will find utility in a broader range of oxidoreductases and beyond.

2. THE CHEMICAL POTENTIAL JUMP

2.1. Theory and Practical Elements. In a μ-jump experiment the chemical potential of a species in the reaction of interest is rapidly altered from its initial equilibrium state (μ^i) through photochemical reactions facilitated by a photosensitizer. At constant temperature and pressure, the molar Gibbs free energy of a chemical reaction is defined by eq 1

$$dG_{T,p} = \sum \mu_X \cdot dn_X \tag{1}$$

where n_X is the stoichiometric coefficient of species X and μ_X is the molar chemical potential, defined in the experimental conditions by eq 2,

$$\mu_X = \mu_X^0 + RT\ln(\gamma_X c_X) \tag{2}$$

with μ_X^0 indicating the standard chemical potential, R the gas constant, T the temperature in Kelvin, γ_X the activity coefficient, and c_X the concentration. It follows then that by changing the concentration of species X from that defined in the initial equilibrium (μ_X^i), the chemical potential will "jump" to μ_X^j causing $\Delta G \neq 0$, resulting in the system evolving to a new final equilibrium (μ_X^f) by catalytic chemical flux to some new species Y (dn_x, Figure 1).

For oxidoreductases initially at equilibrium, a μ-jump can be initiated by a rapid change in substrate, product, oxidant, reductant, or another nonredox cofactor's (e.g., adenosine triphosphate) concentration. In a substrate or product μ-jump, photochemical transformations following light absorption convert an inaccessible "caged" form of the substrate or product to the bona fide reactant. The specificity of substrates and products, as well as the small library of commercially available caged reagents, limit the scope of such μ-jumps. More commonly, a redox μ-jump is employed, where the oxidant or reductant concentration is altered by photochemical ET, and the photosensitizer excited state acts as an oxidant or reductant. Three basic constructions of a redox μ-jump scheme can be conceived (Scheme 1), the photosensitizer can directly reduce (oxidize) the oxidoreductase from the excited state, from the ground state following reductive (oxidative) quenching with a sacrificial electron donor (acceptor), or indirectly, where the redox quencher acts as a mediator of ET between the photosensitizer and the enzyme. The resulting μ-jump to μ_X^j can be expressed as an equivalent electrochemical potential

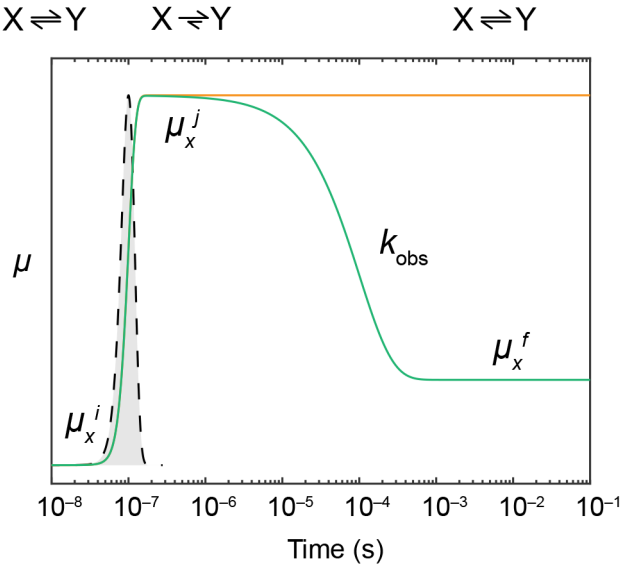

Figure 1. Chemical potential profile of a μ-jump experiment for reaction X ↔ Y. The system is initially at equilibrium (μ^i); then, following an actinic excitation pulse (gray Gaussian, full-width at half-maximum 20 ns), the system jumps to μ^j. In the absence of a catalyst $\mu^j = \mu^f$ (orange), whereas if a catalyst is present, the system evolves to a new equilibrium at $\mu^f \neq \mu^i$ (green) with a rate (k_{obs}) dictated by diffusion and the chemical steps of catalyst.

jump using the Nernst equation and reported in mV from an initial equilibrium.

Each construction of the μ-jump has distinct chemical and energetic landscapes that determine the appropriate kinetic interpretation. When the photosensitizer exchanges electrons with the enzyme directly from the excited state, the μ-jump decays with the excited state. The energetics of ET within this limited temporal window are strongly exergonic since the free energy of the lowest lying emissive excited state (ΔG_{ex}) is often >1.5 eV (λ < 820 nm) for most photosensitizers; the reduction potential of the common photosensitizer tris(bipyridine)-ruthenium(II) excited state couples Ru^{II}*/Ru^{I} and Ru^{III}/Ru^{II}* couples are +0.84 V and −0.84 V vs NHE, respectively.[15,16] Constrained by the excited state lifetime, the rate of ET from the photosensitizer to the oxidoreductase is dictated by diffusion, and the Marcus limit for outer-sphere ET defined by eq 3,

$$k_{ET} = \frac{2\pi}{\hbar} H_{AB}^2 \frac{1}{\sqrt{4\pi\lambda k_B T}} \exp\left[-\frac{(\lambda + \Delta G^\circ)^2}{4\lambda k_B T}\right] \tag{3}$$

where ΔG^0 is the standard Gibbs free energy of ET, λ is the reorganization energy, H_{AB} is the donor−acceptor distance-dependent electronic coupling matrix element, $\hbar$ is Planck's constant, k_B is the Boltzmann constant, and T is the temperature. The free energy of charge recombination, following ET to or from the photosensitizer excited state, is larger than initial ET event, as described by the Rehm−Weller relationship, for example, Ru^{II}/Ru^{I} E^0 = −1.26 V and Ru^{III}/Ru^{II} E^0 = +1.26 V vs NHE.[16,17] As such, charge recombination is competitive with, or faster than ET, and will likely outcompete any enzymatic chemistry of interest. If the reaction is monitored by photosensitizer fluorescence, only forward ET can be extracted from the concentration dependence of emission lifetime or intensity through a Stern−Volmer analysis.[18] Given the sensitivity of fluorescence-based techniques and the theoretical

https://doi.org/10.1021/acscatal.1c04525
ACS Catal. 2021, 11, 14635−14650

Scheme 1. Redox μ-Jump Constructions Including Photosensitizer (PS), Sacrificial Agent (SA), and Oxidoreductase (O)

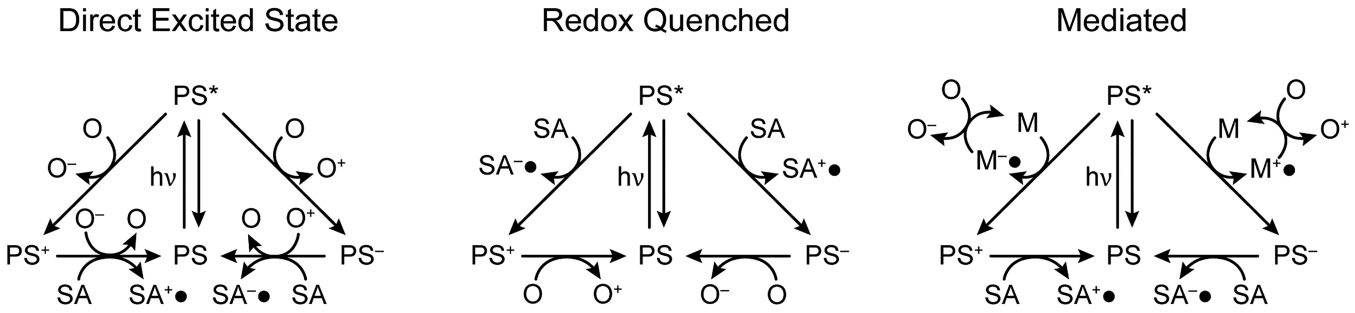

reversibility of the overall reaction, direct excited-state ET is advantageous for the analysis of forward ET step when sample economy is at a premium.

The temporal constraint of a photosensitizer excited-state lifetime and charge recombination, can limit the mechanistic insight of such a redox μ-jump construction. Redox quenching of the photosensitizer by an appropriate sacrificial agent generates a ground state oxidized or reduced photosensitizer for ET with the oxidoreductase of interest, but excited-state relaxation and charge recombination pathways do not contribute to the ensuing kinetics. This simplifies the kinetic interpretation, expands the temporal window of kinetic observation, and increases the flux through subsequent chemical steps. When added in excess, sacrificial agents efficiently "flash-quench" the excited state, avoiding the need for high photosensitizer or enzyme concentrations, the former of which can lead to inhomogeneous μ-jumps across the probe volume due to the inner filter effect. Following excited state ET, a sacrificial agent radical is formed, which generally decays by diffusion-limited chemistry. For instance, a small thiol may be chosen as a sacrificial electron donor to ultimately form a stable disulfide with a modest 2 e^- (2 H^+) reduction potential, yet the initial thiyl radical intermediate is highly reactive[19,20] and may oxidatively reform the sulfhydryl through off-pathway chemistry, form a disulfide with another thiyl radical, or attack a sulfhydryl group, creating a potent disulfide radical anion reductant, resulting in a second ET reaction from a single photon absorption event.[21] The redox quench approach is most appropriate for direct observation of chemical steps that follow ET and may be slower than charge recombination. The large driving force for ET ensures that the observed rate constant for ET represents the forward ET rate constant from photosensitizer to oxidoreductase and that the reaction is driven to completion, maximizing subsequent enzyme intermediate populations.

Direct excited-state or flash-quenched ET from the photosensitizer relies on photosensitizer acting as both light absorber and ET agent. This dual obligation of the photosensitizer may limit the tunability of photophysical properties and efficiency of redox communication with the oxidoreductase of interest. Using a mediator to facilitate ET from the photosensitizer to the oxidoreductase decouples photon capture and redox chemistry, and, like sacrificial agents, a mediator can be added to excess to drive bimolecular ET. Mediators in a μ-jump experiment are distinct from sacrificial agents in that they have reversible one-electron redox couples, for example, viologens or metal complexes, but they precipitate similar reactive photosensitizer species following ET, which must be quenched by a sacrificial agent to avoid charge recombination or off-pathway chemistry.

As the ultimate ET partner for the oxidoreductase in a mediated redox μ-jump, the mediator must be able to exchange electrons with the oxidoreductase of interest, and therefore, it will equilibrate with the oxidoreductase prior to photosensitizer excitation. For mediators with reduction potentials well separated from those of the oxidoreductase cofactors or substrates, or for oxidoreductases that catalyze irreversible chemistry, the mediator can be assumed to start in a single redox state. In a reductive μ-jump of this type, the mediator population starts in the oxidized form (μ^i), and the solution rapidly shifts to some much lower potential defined by an increased reduced mediator population (μ^j). For irreversible enzymes, or for μ-jumps in which the redox couples involved are widely separated and large concentration changes are induced, the rate of approach to the new equilibrium is initially dictated by the forward rate constant(s). However, if a mediator is chosen with a reduction potential close to that of a reversible oxidoreductase, the relaxation rate will be influenced by both forward and reverse ET. This can be particularly useful when information on both the forward and reverse reaction are of interest and is unique to this reaction configuration, but only small (*vida infra*) excursions from equilibrium can be interpreted with confidence.

To understand how μ-jumps near equilibrium can be kinetically modeled consider the two relative equilibria shown in reactions 1 (rxn 1) and 2 (rxn 2).

$$M^{red} + E^{ox} \rightleftharpoons M^{ox} + E^{red} \quad \text{(rxn 1)}$$

$$S + E^{ox/red} \rightleftharpoons P + E^{red/ox} \quad \text{(rxn 2)}$$

where M indicates the μ-jump mediator, E indicates the enzyme and S and P indicate substrate and product, respectively. For a simple bimolecular reaction described in Reaction rxn 1, the rate law that describes the change in concentration of species X ($\Delta[X]$) is described by eq 4,

$$\frac{d\Delta[X]}{dt} = -k_1(([M^{red}]^f + d)([E^{ox}]^f + d)) + k_{-1}(([M^{ox}]^f - d)([E^{red}]^f - d)) \quad (4)$$

where d is defined as the displacement from the final equilibrium concentration $[X]^f$. To linearize this rate equation, it is necessary to have either "small" excursions from equilibrium or for the equilibrium constant (K_{eq}) to be close to 1. Under either condition, the d^2 term can be neglected, and the rate law simplifies to the form in eq 5.[22]

https://doi.org/10.1021/acscatal.1c04525
ACS Catal. 2021, 11, 14635−14650

$$\frac{d\Delta[X]}{dt} = -k_1([M^{red}]^f[E^{ox}]^f) + k_{-1}([M^{ox}]^f[E^{red}]^f) - d(k_1([M^{red}]^f + [E^{ox}]^f) + k_{-1}([M^{ox}]^f + [E^{red}]^f)) \quad (5)$$

The first two terms can be eliminated since they represent equilibrium in the final state, yielding eq 6, with τ defined by eq 7.

$$\frac{d\Delta[X]}{dt} = -(k_1([M^{red}]^f + [E^{ox}]^f) + k_{-1}([M^{ox}]^f + [E^{red}]^f))d = -\left(\frac{1}{\tau}\right)d \quad (6)$$

$$\tau = \frac{1}{k_1([M^{red}]^f + [E^{ox}]^f) + k_{-1}([M^{ox}]^f + [E^{red}]^f)} \quad (7)$$

Integration produces the familiar exponential rate law in eq 5.

$$\Delta[X](t) = \Delta[X]^f \cdot e^{-\tau \cdot t} \quad (8)$$

The observed τ (τ_{obs}) for any species in the equilibrium over a range of concentrations can thus provide the reversible ET rate constants, provided knowledge of K_{eq} from the relevant reduction potentials and solution conditions is available.

When a near equilibrium μ-jump is employed to monitor oxidoreductase chemistry following ET, the kinetic interpretation becomes significantly more complicated but can still be useful. For instance, consider a mediator with a rapid diffusion limited ET pre-equilibrium and a slower subsequent H atom transfer reaction. The initial ET equilibrium can be treated independently with a relaxation rate (τ_1) identical to that of eq 7 and a second relaxation rate (τ_2) defined by eq 9

$$\frac{1}{\tau_2} = k_2\frac{K_1([M^{red}]^f + [E^{ox}]^f}{1 + K_1([M^{red}]^f + [E^{ox}]^f} + k_{-2} \quad (9)$$

representing a pre-equilibrium weighted relaxation rate. Enzymes that operate reversibly and proficiently can be expected to have similar k_n and k_{-n} rate constants, and therefore if $\tau < (2 \times k_{cat})^{-1}$ for the relaxation rate of a defined intermediate the intermediate can be assumed to be kinetically competent to a first approximation.

2.2. Application to Hydrogenases. Hydrogenases are oxidoreductases that catalyze the reversible oxidation of dihydrogen (H_2) and are of significant interest in sustainable biotechnology and biomimetic catalyst design.[23−25] The active sites of hydrogenases harbor unique cofactors that are differentiated by their structure and metal content, denoted [NiFe], [FeFe], and [Fe], a product of convergent evolution, with distinct function in bacterial and archaeal metabolism.[26] Only the [NiFe]- and [FeFe]-hydrogenases catalyze both H_2 oxidation and H^+ reduction, often with distinct biases toward oxidative or reductive catalysis, whereas the [Fe]-hydrogenases use H_2 to reduce methenyltetrahydrobiopterin in methanogens and are not discussed further herein.[27] The [NiFe]- and [FeFe]-hydrogenase active site cofactor structures are shown in Figure 2. Each share several common features including a bimetallic active site anchored to the protein scaffold by at least one cysteine thiolate, unusual CO and CN ligands, and iron−sulfur clusters that aid in electron transfer and storage.

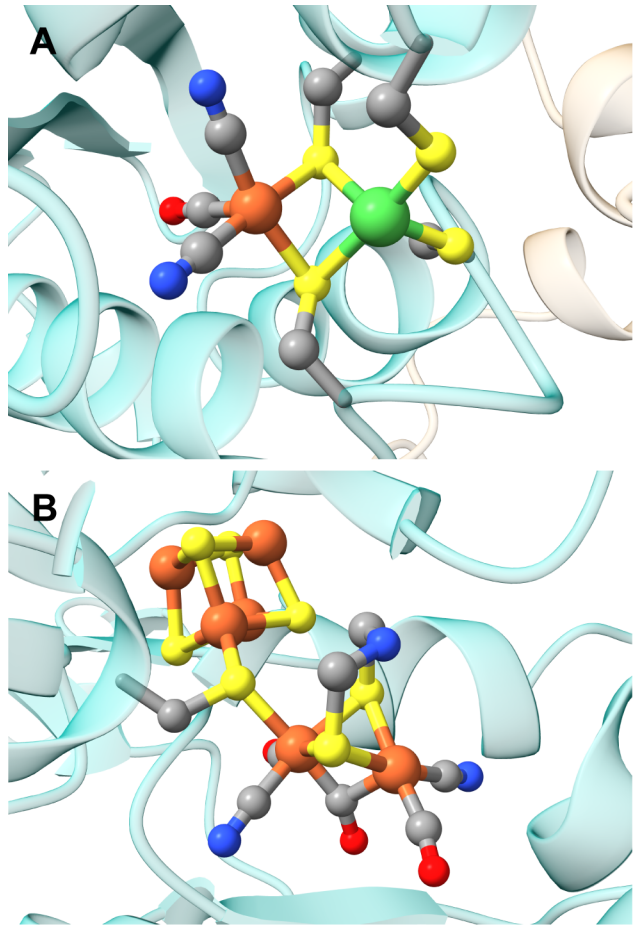

Figure 2. Structures hydrogenase active sites. (A) The membrane-bound [NiFe]-hydrogenase from *Ralstonia eutropha* (PDB 4IUD). The large subunit is indicated in translucent blue and small subunit in translucent tan. (B) The artificially reconstituted [FeFe]-hydrogenase of *Clostridium pasteurianum* (PDB 4XDC). Gray, carbon; blue, nitrogen; red, oxygen; yellow, sulfur; orange, iron; green, nickel.

As a test case for the μ-jump technique, the hydrogenases are particularly fitting, in that they catalyze both H^+ reduction and H_2 oxidation at rates that challenge conventional mixing approaches to mechanistic investigation.[28−31] Prior to the application of μ-jump for rapid initiation, the mechanistic enzymology of both [NiFe]- and [FeFe]-hydrogenases employed two basic types of experiments: equilibrium studies of hydrogenase structure by spectroscopy or X-ray crystallography under various reaction conditions, and kinetic approaches by either solution-based assays or protein film voltammetry. The former developed a set of steady-state intermediates among the two hydrogenases that were chemically competent, and the latter set the time scale necessary to demonstrate kinetic competency. The lack of structural information in kinetic experiments meant that the intermediates identified in steady-state experiments could not be kinetically validated and that potentially fleeting intermediates would elude steady-state identification.

2.2.1. [NiFe]-Hydrogenases. The [NiFe]-hydrogenases are structurally and functionally diverse,[26] but common to all members of this class are two universally conserved large (L) and small (S) subunits that harbor the [NiFe] active site and a chain of three iron−sulfur clusters for electron exchange, respectively. The similarity of this heterodimeric core among the

https://doi.org/10.1021/acscatal.1c04525
ACS Catal. 2021, 11, 14635−14650

diverse [NiFe]-hydrogenase groups, particularly near the [NiFe] site, infers a common mechanism at the active site. Extensive spectroscopic studies reinforce this assertion, where conserved discrete steady states, termed S, C, and R, are observed under conditions consistent with turnover (Figure 3A).[25] The structure of intermediate S is most consistent with

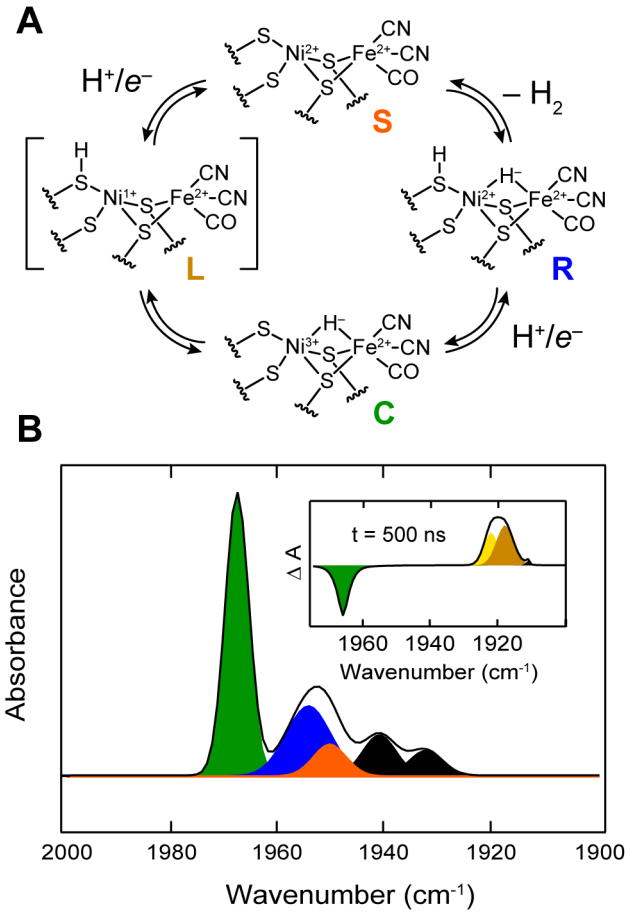

Figure 3. (A) Steady-state intermediates proposed to be involved in the catalytic cycle of [NiFe]-hydrogenases. (B) Steady-state FTIR absorption and postphotolysis (inset) spectra of *Pf*SHI in the carbonyl absorption region. Colors indicate intermediates associated with the cycle in A. Photolysis of C generates two L states. Absorption features in black indicate inactive intermediates. Spectrum taken from refs 43 and 44 with permission.

low-spin divalent nickel and iron with an open coordination site between the metals or a weakly coordinated water.[32,33] Upon proton-coupled reduction of S, the nickel is oxidized by one electron to form a bridging hydride $Ni^{3+}-H^{-}-Fe^{2+}$ C state.[34,35] A second proton-coupled reduction generates at least one $Ni^{2+}-H^{-}-Fe^{2+}$ R state[36] (additional states indicated by R′, R″, etc.) with a putative protonated Ni-terminal cysteine thiol.[37,38] Cryogenic photolysis of the C state, generates a state termed L (Figure 3A), characterized as a formally Ni^{+} species without a detectable bridging hydride, but this species had not been observed under turnover conditions prior to the μ-jump experiments described below.[34,39]

The CO ligand of the active site iron serves as a sensitive reporter of the relative electron density at the [NiFe] site due to its π-back bonding character, which is manifest in the shift of the mid-IR absorption feature of this ligand in the range of 1900−1980 cm^{-1},[36,40,41] and the S, C, R, and L species can be uniquely identified by mid-IR absorption spectroscopy (Figure 3B). Electron donors, including H_2 and small molecule mediators such as methyl viologen (MV), can be used to modulate the population of each intermediate, and this can be followed by Fourier transform IR (FTIR) to examine the equilibrium prior to a μ-jump.

The soluble [NiFe]-hydrogenase from the hyperthermophilic *Pyrococcus furiosus* (*Pf*SHI)[42] was the first to be investigated by the μ-jump method. In addition to the common $\alpha\beta$ core, this hydrogenase also contains an additional two subunits, δ and γ, that contain additional iron−sulfur clusters and a flavin adenine dinucleotide cofactor that couple H_2 oxidation to nicotinamide adenine dinucleotide phosphate ($NADP^+$) reduction. As with most hydrogenases, viologens and other redox dyes are competent for ET at rates that exceed the physiological ET partner, and the *Pf*SHI reaches optimal activity at >100 °C of >10 000 s^{-1} for both H^+ reduction and H_2 oxidation, and ∼60 s^{-1} at 20 °C.[42,43] When prepared under mildly reducing conditions consisting of ∼4% H_2, 10 mM MV ($MV^{2+}/MV^{+\bullet}$ $E^{0\prime}$ = −440 mV), and 12 mM reduced nicotinamide adenine dinucleotide (NADH), the steady-state FTIR spectrum of *Pf*SHI contains contributions from S, C, and R observed at 1950, 1967, and 1954 cm^{-1} respectively (Figure 3B).[43] Control experiments by nanosecond time-resolved visible-pump IR-probe spectroscopy, in the absence of a photosensitizer or mediator, also identified two L state products of C photolysis at 20 °C at 1922 and 1917 cm^{-1} (Figure 3B, inset) that relaxed back to C rapidly with k_{obs} of 2×10^5 s^{-1}.[43] The equilibrium between S, C, and R is pH dependent in the range of 6.0−9.5, consistent with the previously observed pH dependence of these equilibria in other [NiFe]-hydrogenases.[25,44] At pH 7, the solution reduction potential (μ^i) is set by the hydrogenase-catalyzed equilibrium between the dissolved H_2, H^+, and $MV^{2+/+}$; at 4% H_2 this corresponds to −340 mV vs NHE.

The initial construction of the μ-jump with *Pf*SHI involved the photoionization of NADH by two-photon ionization with an Nd:YAG laser operating at 355 nm.[43] The photoproducts of NADH photoionization are solvated electrons and $NADH^{+\bullet}$/$NAD^{\bullet}$ radicals, all of which have extremely low reduction potentials,[45] and excess MV^{2+} rapidly quenches these reactive species, resulting in a $MV^{+\bullet}$-mediated μ-jump and an NAD^+ photoproduct. In these studies, the ensuing bimolecular ET following the μ-jump was monitored by nanosecond time-resolved visible absorption, following the $MV^{+\bullet}$ absorption band at 635 nm. Based on the transient absorption data shown in Figure 4, the μ-jump achieved by this approach was −50 mV (−390 mV), and the mediator $MV^{+\bullet}$ persisted for >100 ms in the absence of *Pf*SHI. When *Pf*SHI was present, the level of $MV^{+\bullet}$ at the earliest times investigated was lower than the controls by 50 μM, which was attributed to reduction of *Pf*SHI directly by solvated electrons or the $NAD(H^+)^{\bullet}$ species. The difference in the μ^i_{MV+} between the control and *Pf*SHI suggested that the enzyme was reduced by the initial photoproducts of NADH photoionization that competed with MV^{2+}, which is unsurprising given the relative concentrations. The $MV^{+\bullet}$ decay was biexponential with $k_{obs1} = 1 \times 10^3$ s^{-1} and $k_{obs2} = 2 \times 10^2$ s^{-1}. The μ-jump in these experiments were too large to be considered near equilibrium and thus could not be explicitly modeled by relaxation kinetics, likely explaining the apparent biexponential behavior of the decay. Nevertheless, the initial reduction of *Pf*SHI by photoionization products and the subsequent reduction by $MV^{+\bullet}$ both occur faster than the k_{cat}

https://doi.org/10.1021/acscatal.1c04525
ACS Catal. 2021, 11, 14635−14650

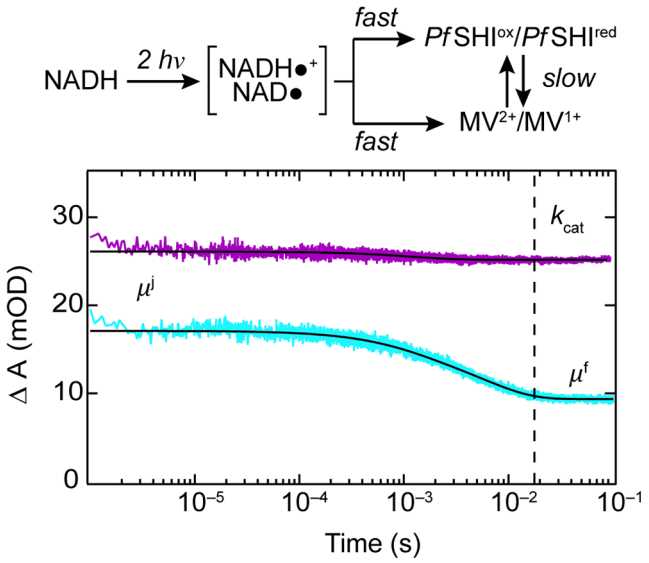

Figure 4. Photochemical mechanism of μ-jump (top) and μ-jump dynamics (bottom) probed by $MV^{+\bullet}$ transient absorbance at 635 nm following excitation at 355 nm. The purple trace shows data from a sample of deoxymyoglobin, used for normalizing the inner filter effect. The cyan trace shows data from a sample containing SHI. Data taken from ref 43 with permission.

of the enzyme under similar conditions. This was the proof of principle necessary to begin mechanistic investigations of steady-state intermediate interconversion on the subturnover time scale.

After intermolecular ET from the mediator to a surface exposed iron−sulfur cluster in *Pf*SHI, the μ-jump equilibrates intramolecularly, and the ET to the [NiFe] active site could be observed by nanosecond time-resolved mid-IR absorption tuned to the fingerprint S, L, C, and R carbonyl resonances. Performed in tandem with the transient visible absorbance, the time-resolved IR data following the S state demonstrated reduction of the active site with biexponential kinetics, $k_{obs1} = 2 \times 10^4\ s^{-1}$ and $k_{obs1} = 5 \times 10^2\ s^{-1}$. The fast reduction rate was pH-dependent. However, the slower phase was not, and subsequent kinetic isotope effect (KIE) and mutagenesis studies established the fast phase corresponded to a concerted orthogonal PCET reaction, where the electron was donated by the proximal $[Fe_4S_4]$ cluster, and the H^+ donated by a conserved glutamate (E_{17} in *Pf*SHI numbering) with a pK_a of ∼7 and significant involvement of nuclear tunneling.[44,46,47] The immediate PCET product was identified to be intermediate L, the two forms of which were in rapid equilibrium, which was followed by tautomerization to form C. This mechanistic proposal was buttressed by contemporary cryogenic work showing photolysis of C to L could lead to accumulation of S if the proximal $[Fe_4S_4]$ cluster was oxidized,[48] as well as subsequent spectroelectrochemical studies at very high pH which demonstrated dark accumulation of L in solution.[49]

Complete reduction of the active site requires a second proton-coupled reduction step from C to R, which exhibited distinct kinetic behavior from that observed in the S to C transition. The C state decay ranged from 200 to 300 s^{-1} and showed little dependence on pH or solvent isotope composition. Formation of R was concerted at pH 6.3, but slowed at higher pH values tested and was interpreted to indicate an ET-PT stepwise mechanism for PCET. Attempts were made to directly observe this intermediate, but were unsuccessful. This observation is consistent with the stability of the Ni^{2+} oxidation state in both S and R, and the high pK_a expected for the Ni^{3+}-bound thiolates relative to the Ni^{2+}.

In the steady state, under conditions similar to those of the μ-jump experiments, the observed KIE for H^+ reduction is 2.6 for the *Pf*SHI. Surprisingly this steady-state KIE is similar to many other [NiFe]-hydrogenases of different classes over a broad range of solution pH.[50] These steady-state properties are inconsistent with the observed rate constants of intermolecular mediator-based ET, intramolecular ET, or *Pf*SHI intermediate interconversions during reductive μ-jumps. What then is the rate-determining step during steady-state turnover? The formation of a nickel- or iron-bound H_2 adduct or H_2 release appear to be most consistent with the available experimental data for this and other hydrogenases as well as some theoretical investigations.[47,51−54]

The above μ-jump studies provide chemical insight into the mechanism of H^+ reduction by [NiFe]-hydrogenases with elementary detail, illustrate their mechanistic flexibility to optimize sequential PCET steps, and demonstrates the value of this approach in extracting detailed mechanistic insight into chemical events that occur significantly faster than k_{cat}. However, the intermolecular ET rates of the $MV^{+\bullet}$ mediator and high fluency UV irradiation necessary for photoionization of NADH limit the applications of such an approach. This has been remedied by the development of a broader range of mediators with different redox potentials[55] and nanoparticle photosensitizers[47,55,56] that can be excited in the visible region of the spectrum and efficiently generate charge separated states. These improvements have expanded the temporal window following hydrogenase reduction by orders of magnitude.

2.2.2. [FeFe]-Hydrogenases. The [FeFe]-hydrogenases exhibit a stronger bias for H^+ reduction than their [NiFe] counterparts, and exceptionally high turnover rates.[25,29] The [FeFe]-hydrogenase active site is composed of a CO- and CN-ligated diiron core with a bridging azidodithiolate proton relay, connected to a $[Fe_4S_4]$ cluster via a shared cysteine thiolate ligand, collectively termed the H-cluster (Figure 5). The iron involved in coordination chemistry with the substrate is denoted

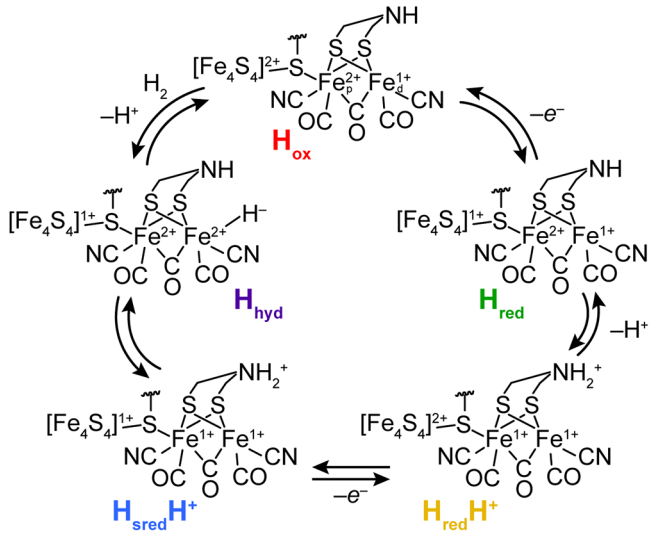

Figure 5. Proposed steady-state intermediates in the catalytic cycle of [FeFe]-hydrogenases.

https://doi.org/10.1021/acscatal.1c04525
ACS Catal. 2021, 11, 14635−14650

as the distal iron (Fe_d), whereas the iron bound to the bridging cysteine is referred to as the proximal iron (Fe_p). As with the [NiFe]-hydrogenases several common intermediates have been observed in the steady state by electrochemical or chemical titrations, yet significant debate remains regarding the proper electronic assignment of the intermediates and their involvement in the mechanism.[57−60] The most oxidized chemically competent steady state is H_{ox}, generally agreed to have an H-cluster composed of a $[Fe_4S_4]^{2+}$ cluster and a mixed valence $Fe_p^{II}Fe_d^{I}$ diiron center with a vacant distal iron coordination site.[25] Reduction of H_{ox} occurs by PCET or ET to generate either $H_{red}H^+$ and H_{red}, respectively, and reduction of $H_{red}H^+$ produces tautomers H_{hyd} and $H_{sred}H^+$,[60,61] where H_{hyd} is poised for H_2 formation and release following a final PT step. Principal mechanistic issues of interest include the stability of stepwise PCET intermediates along the reaction coordinate from H_{ox} and the kinetic relevance of various tautomeric states.

Initial attempts to evidence pre-equilibrium steps in the electron bifurcating HydABC [FeFe]-hydrogenase from *Thermotoga maritima* (*Tm*Hyd)[62] were conducted similarly to the initial *Pf*SHI μ-jump experiments, where NADPH photoionization, in this case, produces solvated electrons, NADP-$(H^+)^\bullet$, and $MV^{+\bullet}$.[63] The H_{ox} state was clearly identified in the steady state prior to μ-jump by FTIR spectroscopy with CO bands at 1939 and 1965 cm^{-1}, as well as CO features assigned to H_{red} (1888, 1931 cm^{-1}) and $H_{sred}H^+$ (1888, 1921, and 1954 cm^{-1}). Transient absorption following the μ-jump demonstrated that *Tm*Hyd was reduced by photoionization products or the $MV^{+\bullet}$ mediator with a rate constant 2×10^3 s^{-1}, 2 orders of magnitude faster than the steady-state $MV^{+\bullet}$ mediated H_2 production rate of the native purified enzyme.[62] It is worth noting that a recombinant expression and maturation protocol for *Tm*Hyd yielding enzyme with ∼5× higher activity has been realized and that the intermediate initially identified as H_{sred} in the original μ-jump studies on the natively expressed enzyme likely corresponds to $H_{red}H^+$.[64] The ensuing active site dynamics probed by transient IR absorbance showed a delay between $MV^{+\bullet}$ oxidation and H_{ox} reduction, which occurred with a rate constant of 1×10^2 s^{-1}. This delay between mediator oxidation and active site reduction implicates a slow intramolecular ET or PT necessary for H-cluster reduction. Formation of the reduced $H_{red}H^+$, the one electron reduced state, was biphasic with rate constants 6×10^3 s^{-1} and 2×10^2 s^{-1}. The faster formation of $H_{red}H^+$ relative to H_{ox} decay is not easily explained, but the spectral congestion and relatively poor quality of the enzyme initial state make detailed interpretation challenging. The main conclusion that could be drawn from this study was the rates of all steps were faster than the steady-state turnover rate, demonstrating kinetic competency of PCET during the H_{ox} to $H_{red}H^+$ transition.

The [FeFe]-hydrogenase from *Chlymadomonas reinhardtii* (*Cr*HydA1),[65] unlike that of *Tm*Hyd, is structurally modest, containing only the H-cluster cofactor,[66] can be efficiently produced and reconstituted artificially,[67] and has been exhaustively characterized, making it a more robust candidate for mechanistic breakthroughs by the μ-jump method. Leveraging the improvements in both photosensitizer and mediator described above, the *Cr*HydA1 was examined by μ-jump initiated time-resolved IR spectroscopy.[57] In this study, a CdSe:CdS "dot-in-rod" nanoparticle structure capped with mercaptopropionic acid ligands served as the photosensitizer (Figure 6A). The ET mediator 2,2′-propyldipyridinium (E° = −550 mV), is dicationic, and thus electrostatically preassociates

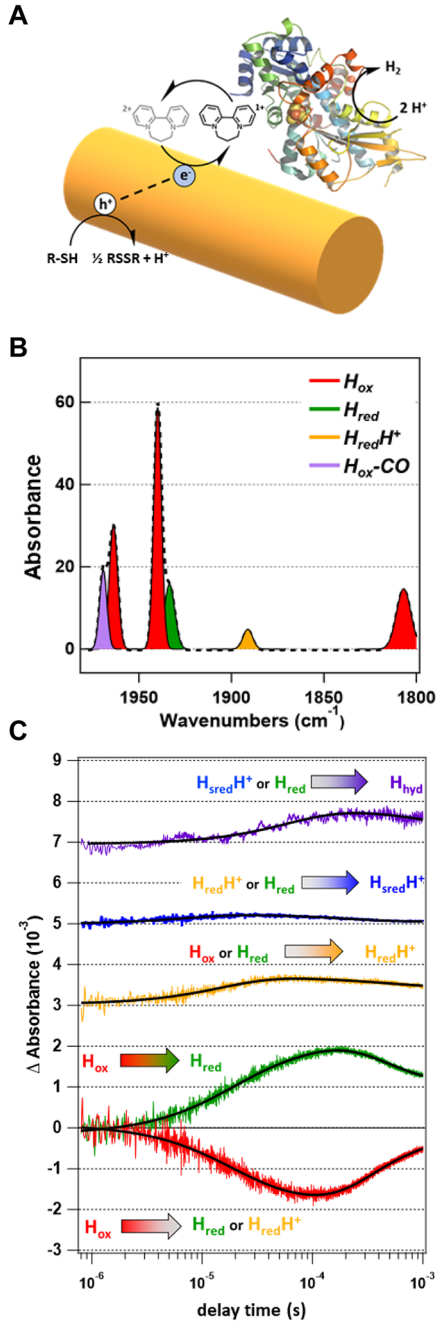

Figure 6. Mechanistic interrogation of CrHydA1 by redox μ-jump. (A) Cartoon of redox μ-jump scheme. Gold rod indicates CdSe:CdS dot-in-rod nanoparticle, which photochemically reduces the 2,2′-propyldipyridinium mediator for ET with CrHydA. (B) Steady-state FTIR spectrum of CrHydA prior to μ-jump. (C) Single wavelength time-resolved IR transients for various intermediates based on their characteristic CO absorption peak. Adapted from ref 57 with permission.

with the anionic nanoparticle ensuring that charge separation quantum efficiencies approach unity.[55,56] The hole, generated following charge separation from the nanoparticle, is refilled by oxidation of surface ligands, ultimately generating disulfides, and surface ligands are regenerated from excess mercaptopropionate in solution. Transient visible absorption following nanoparticle excitation revealed 400−500 μM pyridinyl radical formation in the μ-jump which decayed in the presence of *Cr*HydA1

https://doi.org/10.1021/acscatal.1c04525
ACS Catal. 2021, 11, 14635−14650

biphasically with rates of 6×10^4 s^{-1} and 2×10^4 s^{-1}. The observed biexponential decay kinetics are likely due to the intermediate nature of the μ-jump, which is not expected to relax monoexponentially. The steady-state enzymatic k_{cat} under similar conditions was measured to be $1-0.5 \times 10^3$ s^{-1},[57,68] leaving ample time following *Cr*HydA1 reduction prior to turnover for intermediate observation.

As judged by the steady-state FTIR spectrum, the H-cluster redox state of *Cr*HydA1 was heterogeneous, containing CO resonances consistent with H_{ox}, H_{red}, and $H_{red}H^+$ (Figure 6B). Following the μ-jump, H_{ox} decayed in an intermolecular ET-limited manner concomitant with H_{red} and $H_{red}H^+$ formation (Figure 6C). Assuming H_{red} and $H_{red}H^+$ differ by protonation of the H-cluster, this observation suggests a rapid stepwise ET-PT mechanism with a product distribution dictated by the solution pH. The kinetics of the intermediary species H_{red}, $H_{red}H^+$, and $H_{sred}H^+$ were more complicated based on the flux into and out of these intermediates during the μ-jump relaxation. Following ET-limited formation of H_{red} and $H_{red}H^+$, both intermediates decayed with a rate of 2×10^3 s^{-1}, presumably to $H_{sred}H^+$ or H_{hyd}, yet the formation of $H_{sred}H^+$ was observed to also be ET-limited. H_{hyd}, the state poised for H_2 formation was the slowest to form, but was still close to the intermolecular ET-limit. These observations make each intermediate kinetically viable in mechanistic considerations. Interestingly, the H_{hyd} state was observed to decay with concerted formation of H_{ox} with a rate of 1×10^3 s^{-1}, nearly identical to the steady-state turnover rate, indicating that H_2 formation or release is rate determining in this [FeFe]-hydrogenase. While more evidence is needed to assign this step as H_2 release, H_2 release is also proposed to be rate-determining in the [NiFe]-hydrogenases, which would represent a remarkable outcome of convergent evolution.

2.3. Opportunities and Limitations. The application of μ-jumps for rapid initiation of hydrogenase catalysis has profoundly informed the mechanistic understanding of these remarkable enzymes, revealing the similarities and distinctions between the [NiFe] and [FeFe] forms. Most, if not all, hydrogenases are redox promiscuous, and exchange electrons with small molecule electron carriers or electrodes via iron−sulfur clusters near the protein surface. This promiscuity is a biproduct of their biological function, linking H_2 to metabolism by ET with common electron carrier proteins and cofactors. Electron carrier proteins, for example, copper proteins, cytochromes, and iron−sulfur proteins, act as electron couriers in metabolism, transferring electrons across diverse protein−protein interfaces at sufficient rates to maintain life.[69] It follows that oxidoreductases whose *in vivo* electron donor or acceptor is an electron carrier protein are well suited for rapid initiation by μ-jump techniques.

Several mechanistic questions remain unresolved in oxidoreductases of significant interest that display promiscuous intermolecular ET. Carbon monoxide dehydrogenases and formate dehydrogenases catalyze the reversible reduction of CO_2 to CO and HCO_2^-, respectively, with exquisite selectivity over the thermodynamically more favorable reduction of H^+. The enzymatic properties that encode this chemical selectivity remain to be fully elucidated but are of significant interest for synthetic CO_2 reduction catalyst design to avoid Faradaic losses to H^+ reduction. Selectivity in both formate dehydrogenase and carbon monoxide dehydrogenases does not come at the cost of kinetic rate; both enzymes catalyze CO_2 reduction under ideal conditions at $\geq$500 s^{-1}. For a multiproton, multielectron reaction, this means that each of the elementary steps along the reaction coordinate are at or beyond the time resolution of conventional mixing approaches, making redox μ-jumps a particularly useful alternative. Similar standing challenges and opportunities for μ-jump contributions to mechanistic enzymology abound in other oxidoreductases that are catalytically proficient, for example, cytochrome c nitrite reductase (*E. coli* $k_{cat} > 1 \times 10^3$ s^{-1})[70] or cytochrome c oxidase (*S. cerevisiae* $k_{cat} > 1 \times 10^3$ s^{-1}).[71]

Methodological improvements in optically triggered redox μ-jump promise to broaden the scope and value of the μ-jump technique to diverse oxidoreductases. Toward this end, mediated μ-jumps offer the most flexibility as the photophysical properties of the photosensitizer can be synergistically optimized with the ET mediator independently. Development of new mediators with varied reduction potentials, structural and electrostatic properties, as well as photosensitizers with improved charge separation and optical properties will expand the scope of the mediated μ-jump method in the study of oxidoreductases with promiscuous ET.

Many oxidoreductases do not carry intrinsic redox active cofactors, but instead use soluble electron carrying cofactors to reduce or oxidize their substrate in a ternary complex. The electron carriers and substrates in these types of oxidoreductases generally catalyze concerted two electron transfer reactions through hydride transfer or disulfide exchange. Since the one-electron reduced or oxidized intermediate is not relevant to the native reaction coordinate, the single electron chemistry described in the μ-jump methods may not inform on the native mechanism. This should not be taken to mean that this type of oxidoreductase chemistry is inaccessible by μ-jump methods. In the study of [NiFe]- and [FeFe]-hydrogenases, photoionization of NAD(P)H generated a reduced mediator and $NAD(P)^+$. If a redox mediator is chosen to sacrificially absorb electrons in the irreversible photoionization process, a rapid oxidative μ-jump can be achieved by changing via $NAD(P)^+$. Similar strategies can be conceived for rapid initiation of other oxidoreductases with concerted two-electron transfer reactions.

Most, if not all oxidoreductases catalyze proton-coupled redox transformations, and a $[H^+]$ μ-jump (pH jump) may be an alternative or complementary approach to study oxidoreductase mechanism. In a pH jump, the concentration of protons is rapidly photochemically altered, and all proton-coupled redox equilibria will be shifted based on the Nernstian behavior of proton-coupled reactions.[72] Several photoacids, molecules that release a proton from their excited state or photochemically decompose to form an acidic or basic functional group, have been developed that can be deployed for pH jump-based rapid initiation.[73] The rapid diffusion of H^+ in aqueous solution also make this approach to studying fast redox events appealing. Enzymes are evolutionarily optimized to their cellular environment which have a distinct and homeostated pH. These properties should be carefully considered when designing a pH jump experiment. In a similar spirit, other caged reagents have been developed, including caged ATP,[74] that can rapidly generate μ-jumps. Photochemical ATP μ-jumps are broadly applicable in enzymology, where many enzymes use ATP to power energetically demanding reactions, but oxidoreductases may not be the most obvious enzyme class of opportunity. Nonetheless, nitrogenase and benzoyl-coenzyme A reductase couple ATP hydrolysis to ET, and thus, photochemical release of ATP in the presence of reductant could rapidly initiate chemistry in these oxidoreductases.[75,76] Phosphate release following hydrolysis is proposed to be rate determining in the

https://doi.org/10.1021/acscatal.1c04525
ACS Catal. 2021, 11, 14635−14650

molybdenum−iron nitrogenase of *Azodobacter vinelandii*; thus, an ATP μ-jump could be used to investigate presteady-state phenomena, including the ATP hydrolysis-independent ET between the iron protein and the molybdenum−iron protein.[77]

In both μ-jump studies of [NiFe]- and [FeFe]-hydrogenases, a specialized tandem nanosecond resolved transient IR/visible absorption spectrophotometer was employed to follow mediator limited ET and active site dynamics. The IR probe was particularly useful for monitoring the biologically unusual CO ligands of the active site. Transient IR absorption spectroscopy of even modest time resolution requires specialized instrumentation and is an inherently low sensitivity technique. For these reasons, it may not be appropriate for other oxidoreductases of interest. Alternatively, nanosecond resolved transient visible absorption systems are commercially available, common in physical chemical laboratories, and may offer superior sensitivity. This increased accessibility and sensitivity comes at the cost of spectral congestion; selective photosensitizer stimulation and background-free observation of ET and enzymatic chemistry may be limited by the optical properties of the species under investigation.

3. ARTIFICIALLY PHOTOSYNTHETIC ENZYMES

Artificially photosynthetic oxidoreductases are nonphotosynthetic oxidoreductases that are associated with a photosensitizer such that light absorption can be coupled to catalysis.[78−80] The advantage of using an artificially photosynthetic enzyme is that the rate of ET between photosensitizer and oxidoreductase is no longer dependent on diffusion, thus significantly expanding the temporal window available for mechanistic study, even at low concentration and light fluence. Following charge transfer across the protein-photosensitizer interface, charge recombination must be suppressed in order to observe catalytic chemistry by the addition of a sacrificial agent, similar to the μ-jump approach.

The attachment of the photosensitizer to the enzyme can be accomplished either covalently or noncovalently. For covalent attachment of the photosensitizer to the oxidoreductase, a reactive surface exposed canonical or noncanonical amino acid may be targeted for ligation to a synthetic photosensitizer, a strategy originally pioneered in the study of ET in metalloproteins.[81] While canonical thiol- and amine-containing amino acid side chains are most common for covalent attachment, their ubiquity can make selective assembly challenging; genetic code expansion offers a roadmap to more selective protein conjugation by site-specifically expanding the reactivity of amino acid side chains for covalent assembly. Alternatively, endogenous cofactors of the enzyme, such as iron−sulfur clusters, can bind photosensitizers by substitution of one of the anchoring protein cysteines for a noncoordinating amino acid and installing a sulfhydryl group on the photosensitizer for direct attachment. Examples of covalently assembled artificially photosynthetic enzymes include ribonucleotide reductase (RNR) photosensitized by a single non-native cysteine linked rhenium(I) 1,10-phenanthroline tricarbonyl methylpyridine chromophore,[82] [NiFe]-hydrogenase linked nonspecifically through aspartate/glutamate amide bonds to a ruthenium bis-2,2′-bipyridine 5-amino-1,10-phenanthroline chromophore,[83] cytochrome P450 linked through a single non-native cysteine residue to a ruthenium bis-2,2′-bipyridine 5-amino-1,10-phenanthroline chromophore,[84] and even [FeFe]-hydrogenase linked by a various linear alkyl dithiols to photosystem I between the terminal [Fe_4S_4] clusters.[85]

Covalent attachment of a photosensitizer to an oxidoreductase may require significant protein engineering, reaction condition optimization, and additional purification steps that may not be compatible with all oxidoreductases of interest. In this case, the adsorption of the oxidoreductase to the photosensitizer driven by noncovalent interactions may be advantageous.[78−80] Various oxidoreductases, including several hydrogenases,[86−89] formate dehydrogenase,[90] carbon monoxide dehydrogenase,[91] and even nitrogenase[92] have been catalytically driven by adsorbed dyes, quantum dots, or carbon-based nanoparticle materials.[93] Among them, most of the aforementioned noncovalent assemblies are driven by electrostatic interactions between nanoparticle surface ligands and areas of net complementary charge on the protein surface that may mimic the interactions of the oxidoreductase and their ET partner protein. Protein−ligand and hydrophobic interactions have been less exploited, but may also be effective in assembling photosensitizer-protein hybrids. Despite their ubiquity in biophotocatalytic applications, only a few studies have leveraged the noncovalent photosensitized oxidoreductase assembly for light-initiated mechanistic investigations, particularly at the active site.[87,94]

To interpret fast ET kinetics in covalent assemblies it is necessary for there to be a uniform photosensitizer-enzyme assembly, since the environment and donor−acceptor distance affect the Marcus parameters of the ET kinetics. Homogeneous photosensitized enzyme assemblies must also retain functional fidelity, and not interfere with the catalytic chemistry of the enzyme. The design of a homogeneously functionalized artificially photosynthetic enzyme and the utility of this approach to interrogate chemical events on a range of temporal and spatial scales are described below.

3.1. Ribonucleotide Reductase. As with the hydrogenases, the class Ia ribonucleotide reductase (RNR) from *E. coli* offers a prescient example of the utility of rapid initiation in oxidoreductase enzymology as an artificially photosynthetic construct. All organisms rely on RNR for the *de novo* production of deoxynucleotides necessary for DNA biosynthesis and repair, where RNR catalyzes the reduction of nucleoside di- or triphosphates to the corresponding deoxynucleotide by a thiyl radical-based mechanism.[3,95] The thiyl radical is transiently generated on every turnover, and the mechanism of thiyl radical generation forms the basis for classification of RNRs; class I use a second protein that harbors a stable amino acid radical or metal oxidant, class II use the 5′-deoxyadenosyl radical formed during adenosylcob(II)alamin Co−C homolysis, and class III harbor a stable glycyl radical adjacent to the catalytic cysteine. The *E. coli* RNR forms a transient catalytic $\alpha_2\beta_2$ structure, where α is the subunit that carries out nucleotide reduction and allosteric regulation, and β harbors a stable diiron tyrosyl radical necessary for thiyl radical formation in α. Upon $\alpha_2\beta_2$ assembly (Figure 7A), with the appropriate nucleoside diphosphate (NDP) substrate and nucleotide allosteric effector, conformationally gated radical transfer is initiated from the tyrosyl radical in one β subunit ($Y_{122}^{\bullet}$, *E. coli* numbering) 34 Å to the active site cysteine thiol in α (C_{439}) via a series of PCET steps along a series of redox active amino acids ($Y_{122}^{\bullet}[\beta] \leftrightarrow W_{48}[\beta] \leftrightarrow Y_{356}[\beta] \leftrightarrow Y_{731}[\alpha] \leftrightarrow Y_{730}[\alpha] \leftrightarrow C_{439}[\alpha]$, Figure 7B).[96,97] Once formed, the $C_{439}^{\bullet}$ abstracts a hydrogen atom from the NDP 3′-carbon, and the substrate radical is reduced by two active site cysteines (C_{225} and C_{462}) to the corresponding 2′-deoxynucleotide (dNDP), the thiyl radical is regenerated, and transferred back to Y_{122}, completing the catalytic cycle. Radical transfer chemistry is fast

https://doi.org/10.1021/acscatal.1c04525
ACS Catal. 2021, 11, 14635−14650

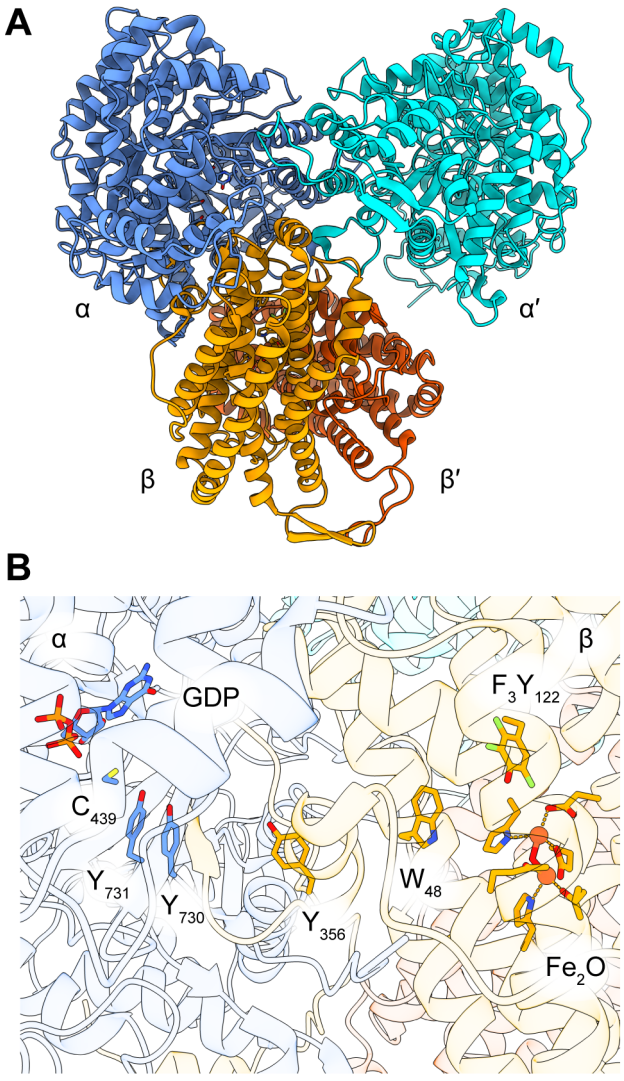

Figure 7. Cryo electron microscopy structure of wild type α_2 $E_{52}Q$:$Y_{356}F_3Y$ β_2 *E. coli* RNR (PDB 6W4X). (A) Asymmetric quaternary structure. (B) Radical transfer pathway residues, diiron cofactor, and substrate GDP.

($>10^3$ s^{-1}) relative to conformational gating (10 s^{-1}) and active site disulfide rereduction; thus, in both steady-state and conventional presteady-state kinetic experiments, no pathway or substrate radical accumulates.[98] Extensive mutagenesis studies targeting the radical transport pathway with both natural and non-natural amino acid substitutions has provided compelling evidence for the identity and fidelity of the radical transport path, and the structure of the radical intermediates therein, but radical formation and decay are limited by conformational dynamics that occur orders of magnitude slower.[99−101] The conformational gating of radical transfer is likely critical for protecting the tyrosyl radical from reduction *in vivo*, but has obscured the direct study of PCET along the radical transfer pathway and active site chemistry.

Photosensitization of RNR has been proposed and shown to overcome the time resolution barrier imposed by conformational gating of radical transfer for mechanistic study. An artificially photosynthetic $\alpha_2\beta_2$ RNR complex can be preassociated and conformationally poised for radical transfer, and photochemical "seeding" of a pathway radical would initiate radical equilibration along the pathway. Early attempts to design a photochemical RNR relied on covalent attachment of a photooxidant to a small peptide analogue of the β C-terminus that largely dictates $\alpha_2\beta_2$ binding. The photooxidant was installed site specifically at the N-terminus directly adjacent to Y_{356} in the 20-mer peptide by a peptide bond and several photooxidants were examined including tryptophan,[102] benzophenone,[103] anthroquinone,[104] and a rhenium bipyridyl complex.[104] Excitation of the photooxidant stimulated ET or PCET from the Y_{356} equivalent in the peptide to the chromophore, creating a charge transfer complex and a spectroscopically detectable $Y^\bullet$ that was chemically competent for nucleotide reduction. Despite direct evidence of a $Y^\bullet$ in the peptide in complex with α, spectral congestion with the photooxidant and the multitude of tyrosines both on and off the radical transfer pathway that could be oxidized photochemically precluded kinetic investigations of PCET along the pathway.

The assembly of a covalently labeled photoβ_2 proved to be a major breakthrough in mechanistic investigations of PCET in RNR.[82] By mutating the only two surface exposed cysteines in the native β_2 to serine ($C_{268}S$ and $C_{305}S$), and the serine adjacent to Y_{356} to cysteine ($S_{355}C$), a single sulfhydryl group could be targeted for labeling proximal to the radical transfer pathway. Reacting the reduced iron loaded mutant photoβ_2 with a 4-bromomethyl pyridyl-ligated rhenium(I) 1,10-phenanthroline tricarbonyl complex ($[Re]^I$) generates the photosensitized holophotoβ_2 by nucleophilic substitution with a ligand-to-metal charge transfer band at 375 nm. Excitation of the $[Re]^I$ chromophore forms $[Re]^{I*}$, the emissive lifetime of which is shortened in photoβ_2 relative to the redox inert $Y_{356}F$ photoβ_2, implying that photochemical oxidation of the adjacent radical transfer pathway tyrosine occurs on the nanosecond to microsecond time scale. To examine the tyrosyl radical directly, charge recombination has been suppressed by using the sacrificial electron acceptor ruthenium(III) hexamine, oxidatively quenching $[Re]^{I*}$ to $[Re]^{II}$, which was shown spectroscopically to oxidize Y_{356} along with a small fraction of off-target aromatic amino acid oxidation.[105] The photochemical tyrosyl radical yield in a photoβ_2 was further improved by the incorporation of fluorotyrosines (F_nYs) in place of Y_{356}, which can systematically vary the reduction potential and pK_a to examine the thermodynamics and kinetics of PCET.[106−108] This flash quenching method for generating $Y_{356}^\bullet$ in photoβ_2 on the nanosecond time scale laid the groundwork for a breadth of otherwise impossible mechanistic studies on radical transport in RNR among the complete pathway in an $\alpha_2$photoβ_2 complex.

When incubated with α_2, substrate, and allosteric effector, the photoβ_2 was shown to bind to α_2 with a K_d of 2 μM, remarkably similar to the native β_2 K_d of 0.2 μM, given the large perturbation of the subunit interface introduced by the [Re] photooxidant.[82] This fortuitous binding affinity of the $\alpha_2$photoβ_2 complex allowed for spectroscopic and kinetic studies on fully complexed α_2:photoβ_2. As with free photoβ_2, emission lifetime kinetics of the [Re] photooxidant in the α_2:photoβ_2 complex were sensitive to the identity of the amino acid at position 356(β), and $Y_{356}^\bullet$ was demonstrated to be the photooxidation product by transient absorption spectroscopy sensitive to the characteristic absorbance of the radical at 412 nm. Once generated, the $Y_{356}^\bullet$ within α_2:photoβ_2 was chemically competent for nucleotide reduction in a pathway-dependent manner, that is, when $Y_{731}F$ or $Y_{730}F$ pathway blocks were introduced into α, no dNDP was formed.[105] Thus, time-resolved emission kinetics were leveraged to examine the photochemical oxidation of pathway residues,

https://doi.org/10.1021/acscatal.1c04525
ACS Catal. 2021, 11, 14635−14650

and transient absorption and product analysis were used to follow the fate of photochemically generated tyrosyl radicals along the radical transfer pathway.

Fluorotyrosyl radicals, particularly the tri- and tetrafluoro-substituted variants, display elevated reduction potentials relative to Y across a wide pH range, biasing forward radical transfer when site-specifically incorporated at $Y_{356}(\beta)$.[108,109] This property, in concert with the increased photochemical radical yield, was leveraged in a 2,3,5-F_3Y_{356} photoβ_2 to evaluate the $F_3Y^\bullet$ decay in the presence of an intact or mutationally inactivated radical transfer pathway, generated by installing redox inert amino acids at key sites along the pathway including $Y_{731}F$ and $C_{439}S$.[110] The $F_3Y^\bullet$ decay was accelerated when the pathway was intact, consistent with rapid radical transfer to the active site and substrate activation. Using a 3′-deuterated CDP substrate, the rate of $F_3Y^\bullet$ decay effectively collapsed to the blocked pathway rate and was interpreted to indicate that substrate H atom abstraction had become rate determining with respect to radical propagation, with a lower limit on the thiyl radical-mediated substrate activation $\geq 1 \times 10^4\ s^{-1}$. This study represented the first mechanistic studies on active site chemistry achieved by the artificially photosynthetic RNR.

The role of the protein environment in tuning the energetics of (PC)ET is a question of fundamental importance in oxidoreductase function, yet it has been challenging to study in detail by methods not initiated by light. The artificially photosynthetic RNR has been employed for the study of PCET dynamics that affect radical transport at the subunit interface.[106] Using a suite of F_nY_{356} substituted photoβ_2s, the reduction potential of the pathway residue 356 could be varied systematically for a Marcus analysis of photochemical oxidation. Using $[Re]^{I}$* emission kinetics within the α_2:photoβ_2 interface for the various F_nY_{356} photoβ_2s, the Marcus parameters associated with photochemical $F_nY_{356}^\bullet$ could be estimated, revealing distinct behavior of the PCET kinetics of Y oxidation relative to ET from deprotonated F_nYs and that ET occurs in the Marcus inverted regime.

Another element of protein structure that affects (PC)ET kinetics and mechanism involves protein conformational motions, both local amino acid fluctuations and longer-range structural dynamics, and the artificially photosynthetic *E. coli* RNR has proven to be an effective platform for investigating the role of several amino acid residues that modulate dynamics (Figure 8). Steady-state studies using 3-aminotyrosine (NH_2Y) as a tyrosine analogue with a 580 mV depressed radical reduction potential[111] evidenced conformational flexibility of Y_{731} in the X-ray structure of $Y_{730}NH_2Y$ α_2.[101] Subsequent paramagnetic resonance investigation of the radical trapped at $NH_2Y_{731}^\bullet$ revealed that an $R_{411}A(\alpha)$ mutation biases Y_{731} toward a "flipped out" conformation where the Y_{731}−Y_{730} hydrogen bonded dyad interface is disrupted and Y_{731} moves toward the subunit interface, but the stacked dyad interface is reformed upon radical transfer to Y_{730}.[112,113] Due to the conformational gating of radical transfer, the relevance of the conformational motion between flipped out and stacked Y_{731} could not be assessed. Using a modified photoβ_2, where the normal photochemical target Y_{356} was mutated to the redox inert F, the photooxidation of Y_{731} across the $\alpha\beta$ interface by $[Re]^{I}$* was investigated by emission kinetics. In the wild type α, oxidation of Y_{731} is not kinetically competitive with $[Re]^{I}$* decay, whereas in $R_{411}A$ α_2, direct photochemical oxidation of Y_{731} occurs with a rate constant of $8 \times 10^5\ s^{-1}$, suggesting that the increased proximity to the photooxidant enabled PCET.[113] Interestingly,

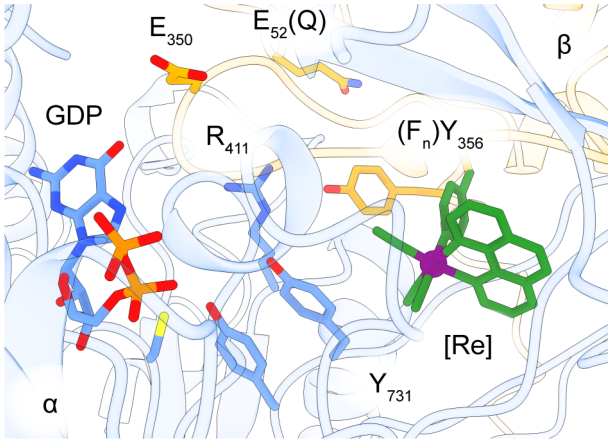

Figure 8. Model of the artificially photosynthetic *E. coli* RNR. The modeled [Re] unit is shown in green with the rhenium atom in purple. Key residues demonstrated to be involved in local or long-range dynamics linked to radical transfer are labeled. Structure based on the cryo-EM structure of the trapped $\alpha_2\beta_2$ complex (PDB 6W4X).

using various pathway block mutations ($Y_{730}F$ and $C_{439}S$), the emission lifetime of $[Re]^{I}$* rose with a more truncated radical transfer pathway, suggesting that Y_{731} conformational dynamics were competitive with $[Re]^{I}$* emission lifetime ($\leq 1\ \mu s$) and that colinear radical transfer was not impaired by the $R_{411}A$ mutation. To examine the effect of the flipped out Y_{731} conformation on radical transfer across the subunit interface from $Y_{356}^\bullet$, a 2,3,6-F_3Y_{356} photoβ_2 was employed as an orthogonal radical probe based on the red-shifted absorption feature of the 2,3,6-$F_3Y^\bullet$ relative to the $Y^\bullet$ background, in complex with ($R_{411}A$) NH_2Y_{730} α_2, which simplified the kinetic model.[113] Using oxidative quenching of the $[Re]^{I}$* state, a clear 2,3,6-$F_3Y_{356}^\bullet$ feature was resolved, and decayed with a rate consistent with orthogonal PCET from $Y_{731}(\alpha)$ to $Y_{356}^\bullet(\beta)$ occurring at $0.6 \times 10^4\ s^{-1}$ for the NH_2Y_{730} α_2. The rate of orthogonal PCET tripled ($1.6 \times 10^4\ s^{-1}$) for the $R_{411}A$ mutant NH_2Y_{730} α_2, indicating that radical transfer was accelerated by the increased proximity of Y_{731} to Y_{356}. Both rates of interfacial PCET, and others derived by analogous methods,[99] were similar to that of hydrogen atom abstraction from the nucleotide substrate, confirming that both long-range PCET and active site chemistry occur much faster than conformational gating.

The nature of the conformational gating step that triggers radical transfer and active site chemistry has remained enigmatic since the earliest kinetic studies on RNR, but necessarily involves allosteric communication between the α and β subunits in the asymmetric complex.[96] Several residues have been identified as highly conserved within the class Ia RNRs within the subunit interface, including E_{350} and E_{52} in β (*E. coli* numbering).[114,115] Modest mutation of either site for Q or D completely abolishes activity and radical transfer, but the mechanistic cause of this loss of activity could not be ascribed based on these data alone, as either residue could be involved in allosteric regulation or PCET directly as a PT partner to a radical transfer pathway residue. The artificially photosynthetic RNR contains a partially truncated radical transport pathway ($Y_{356}\beta$ ↔ $Y_{731}\alpha$ ↔ $Y_{730}\alpha$ ↔ $C_{439}\alpha$), and photochemical radical generation occurs at the interface, thus conformational gating targeting this portion of the pathway, as opposed to $Y_{122}^\bullet$, and the role of PT partner residues at the interface can be assessed. The $E_{350}Q$ photoβ_2 was shown to generate $Y_{356}^\bullet$ by PCET and

https://doi.org/10.1021/acscatal.1c04525
ACS Catal. 2021, 11, 14635−14650

exhibit near native photochemical turnover, demonstrating the kinetic competency of radical transfer from $Y_{356}(\beta)$ to the active site in this otherwise inactive mutant.[116] This photochemical rescue of activity was the basis for the hypotheses that E_{350} is critical in conformational gating that does not target PCET along the radical transfer pathway from Y_{356} to the active site, nor does it affect active site chemistry. It follows that a likely role for E_{350} is in controlling PCET at the endogenous $Y_{122}^{\bullet}$, although this remains to be demonstrated definitively. The E_{52}Q photoβ_2, on the other hand, was inactive in both $Y_{356}^{\bullet}$ photogeneration and substrate reduction.[117] Substitution of Y_{356} for 2,3,5-F_3Y_{356}, which remains deprotonated and thus oxidation is proton decoupled, recovered both photooxidation and photochemical turnover, suggesting that E_{52} is essential in gating PT from Y_{356} during radical transfer by PCET at the subunit interface, among other possible roles. This finding was later supported by computational studies based on the structure of a preturnover α/β pair with an ordered PCET pathway.[96,118]

3.2. Opportunities and Limitations. The use of the artificially photosynthetic RNR has been advantageous for the study of fast events including PCET along the radical transfer pathway and active site chemistry that occur >10^3-fold faster than steady-state turnover. Several elements of this case study are more broadly informative. Many oxidoreductases are intimately integrated into central metabolism, and are thus regulated on several levels including allostery. These regulatory mechanisms can often be challenging to investigate by mutagenesis and traditional enzyme kinetics alone, particularly when the initial events in catalysis are the target of regulation. By targeting an intermediary step, namely the oxidation of Y_{356}, mechanistic investigations could be carried out in mutant enzymes that were otherwise inactive, and it is difficult to imagine an experimental method that could access similar information. Furthermore, many oxidoreductases are dynamic in nature, and may exhibit an ensemble of conformations, both locally and globally, with distinct contributions to the catalytic reaction coordinate. With the increased time resolution afforded artificial photosynthetic constructs, these ensembles can be probed on an expansive time scale dictated by the excited state lifetime of the chromophore. For RNR, conformations observed in the steady state were shown to interconvert faster than turnover, implying little effect on steady-state rates. This will not always be the case for other oxidoreductases, and the chromophore separation from the redox active cofactor can be a sensitive probe of these types of dynamics.

In any artificially photosynthetic enzyme it is important to demonstrate the chemical competency of the photochemical process to ensure the fidelity of the reaction dynamics to the native system. For RNR, the $\alpha_2$photoβ_2 complex is indeed chemically competent as determined by single turnover studies but suffers from markedly lower activity, typically ≤20% of wild type, although the interpretation of this number is somewhat fraught since the ruthenium hexamine oxidative quencher is necessary to increase photochemical yield but inhibits the nonphotosynthetic activity.[106,119] The high reduction potential of both the $[Re]^{I}$* and $[Re]^{II}$ species causes off-pathway amino acid oxidation that is detrimental to both photosynthetic and nonphotosynthetic turnover and should be considered when designing novel artificially photosynthetic constructs.

Nanoparticle-based artificially photosynthetic oxidoreductases offer particular promise as a highly modular photosensitizer. The bulk and structure of many nanoparticles can mimic structural elements of protein−protein interactions, and the tunability of the capping ligand ensemble can further emulate the types of noncovalent interactions influencing ET interfaces. As a proof of concept, the effect of electron delivery rate from mercaptopropionic acid capped CdTe quantum dots to the [NiFe] hydrogenase of *Thiocapsa roseopersicina* as compared to reductively quenched $Ru(bpy)_3^{2+}$ was shown to alter the active site intermediates observed during steady-state illumination, suggesting an interplay between photoreduction and product inhibition.[87] In a similar study, the effect of electron delivery rate from an electrostatically bound CdS quantum dot-nitrogenase complex was investigated, shedding light on how electron delivery rate dictates intermediate build up and H_2 versus N_2 product selectivity.[94]

The unique design of this photochemical construct within a functional RNR subunit interface may not be feasible for other oxidoreductases, but the basic architectural principles and experimental metrics used to evaluate the functionality of the artificially photosynthetic construct should be general. As protein engineering, structural biology, and photosensitizer development continue to progress, artificially photosynthetic enzyme assemblies will likely become more routine, and as with μ-jump initiation methods, when coupled with appropriate time-resolved spectroscopic tools, this strategy for mechanistic investigation of otherwise kinetically masked chemical events in oxidoreductase will continue to advance our understanding of these remarkable enzymes. Unfortunately, only in rare cases is an atomic structure available for the artificial photosynthetic construct, which can hinder informed optimization or kinetic interpretation. Toward improving the structural understanding of these interfaces, cryo-electron microscopy will likely be an invaluable technique.

4. CONCLUSIONS

In the continued quest for new methodologies to better understand enzyme catalysis, rapid initiation techniques have demonstrated their value in overcoming many of the limitations of traditional kinetic approaches to mechanism. Like all methods, both the development of artificially photosynthetic enzymes and the application of a μ-jump require a judicious experimental practitioner, but as more investigators turn to photochemical initiation strategies such as those described herein to probe oxidoreductase mechanisms, technical developments and design simplicity will also emerge. When viewed in the context of developments in structural biology and genetic code expansion, the future is bright for mechanistic enzymology of the oxidoreductases.

AUTHOR INFORMATION

Corresponding Author

Brandon L. Greene − *Department of Chemistry and Biochemistry, University of California, Santa Barbara, Santa Barbara, California 93106, United States;* orcid.org/0000-0001-6981-5900; Email: greene@chem.ucsb.edu

Complete contact information is available at: https://pubs.acs.org/10.1021/acscatal.1c04525

Notes

The author declares no competing financial interest.

ACKNOWLEDGMENTS

I would like to acknowledge Gyunghoon "Kenny" Kang for his modeled structure of the α_2:photoβ_2; my exceptional mentors R.

Brian Dyer, JoAnne Stubbe, and Daniel G. Nocera; and the University of California, Santa Barbara Department of Chemistry and Biochemistry for support.

REFERENCES

(1) Ghosh, A. K.; Samanta, I.; Mondal, A.; Liu, W. R. Covalent Inhibition in Drug Discovery. *ChemMedChem* **2019**, *14* (9), 889−906.
(2) Stancu, C.; Sima, A. Statins: Mechanism of Action and Effects. *J. Cell. Mol. Med.* **2001**, *5*, 378−387.
(3) Greene, B. L.; Kang, G.; Cui, C.; Bennati, M.; Nocera, D. G.; Drennan, C. L.; Stubbe, J. Ribonucleotide Reductases: Structure, Chemistry, and Metabolism Suggest New Therapeutic Targets. *Annu. Rev. Biochem.* **2020**, *89*, 45−75.
(4) Aye, Y.; Li, M.; Long, M. J. C.; Weiss, R. S. Ribonucleotide Reductase and Cancer: Biological Mechanisms and Targeted Therapies. *Oncogene* **2015**, *34*, 2011−2021.
(5) Copeland, R. A. Chance Favors the Perplexed Mind: The Critical Role of Mechanistic Biochemistry in Drug Discovery. *Biochemistry* **2021**, *60*, 2275−2284.
(6) Artero, V. Bioinspired Catalytic Materials for Energy-Relevant Conversions. *Nat. Energy* **2017**, *2*, 1−6.
(7) Bullock, R. M.; Chen, J. G.; Gagliardi, L.; Chirik, P. J.; Farha, O. K.; Hendon, C. H.; Jones, C. W.; Keith, J. A.; Klosin, J.; Minteer, S. D.; Morris, R. H.; Radosevich, A. T.; Rauchfuss, T. B.; Strotman, N. A.; Vojvodic, A.; Ward, T. R.; Yang, J. Y.; Surendranath, Y. Using Nature's Blueprint to Expand Catalysis with Earth-Abundant Metals. *Science* **2020**, *369*, eabc3183.
(8) Le, J. M.; Bren, K. L. Engineered Enzymes and Bioinspired Catalysts for Energy Conversion. *ACS Energy Lett.* **2019**, *4*, 2168−2180.
(9) Yang, Y.; Arnold, F. H. Navigating the Unnatural Reaction Space: Directed Evolution of Heme Proteins for Selective Carbene and Nitrene Transfer. *Acc. Chem. Res.* **2021**, *54*, 1209−1225.
(10) Toogood, H. S.; Scrutton, N. S. Discovery, Characterization, Engineering, and Applications of Ene-Reductases for Industrial Biocatalysis. *ACS Catal.* **2018**, *8*, 3532−3549.
(11) Biegasiewicz, K. F.; Cooper, S. J.; Gao, X.; Oblinsky, D. G.; Kim, J. H.; Garfinkle, S. E.; Joyce, L. A.; Sandoval, B. A.; Scholes, G. D.; Hyster, T. K. Photoexcitation of Flavoenzymes Enables a Stereoselective Radical Cyclization. *Science* **2019**, *364*, 1166−1169.
(12) Page, C. C.; Moser, C. C.; Chen, X.; Dutton, P. L. Natural Engineering Principles of Electron Tunnelling in Biological Oxidation−Reduction. *Nature* **1999**, *402*, 47−52.
(13) Wolfenden, R.; Snider, M. J. The Depth of Chemical Time and the Power of Enzymes as Catalysts. *Acc. Chem. Res.* **2001**, *34*, 938−945.
(14) Kohen, A.; Klinman, J. P. Enzyme Catalysis: Beyond Classical Paradigms. *Acc. Chem. Res.* **1998**, *31*, 397−404.
(15) Bock, C. R.; Connor, J. A.; Gutierrez, A. R.; Meyer, T. J.; Whitten, D. G.; Sullivan, B. P.; Nagle, J. K. Estimation of Excited-State Redox Potentials by Electron-Transfer Quenching. Application of Electron-Transfer Theory to Excited-State Redox Processes. *J. Am. Chem. Soc.* **1979**, *101*, 4815−4824.
(16) Creutz, C.; Sutin, N. Electron-Transfer Reactions of Excited States. Reductive Quenching of the Tris(2,2′-Bipyridine)Ruthenium-(II) Luminescence. *Inorg. Chem.* **1976**, *15*, 496−499.
(17) Rehm, D.; Weller, A. Kinetics of Fluorescence Quenching by Electron and H-Atom Transfer. *Isr. J. Chem.* **1970**, *8*, 259−271.
(18) Stern, O.; Volmer, M. Über die Abklingzeit der Fluoreszenz. *Z. Phys.* **1919**, *20*, 183−188.
(19) Dénès, F.; Pichowicz, M.; Povie, G.; Renaud, P. Thiyl Radicals in Organic Synthesis. *Chem. Rev.* **2014**, *114*, 2587−2693.
(20) Zhang, X.; Zhang, N.; Schuchmann, H.-P.; von Sonntag, C. Pulse Radiolysis of 2-Mercaptoethanol in Oxygenated Aqueous Solution. Generation and Reactions of the Thiylperoxyl Radical. *J. Phys. Chem.* **1994**, *98*, 6541−6547.
(21) Surdhar, P. S.; Armstrong, D. A. Reduction Potentials and Exchange Reactions of Thiyl Radicals and Disulfide Anion Radicals. *J. Phys. Chem.* **1987**, *91*, 6532−6537.
(22) Bernasconi, C. F. *Relaxation Kinetics*; Academic Press, 1976.
(23) Dogutan, D. K.; Nocera, D. G. Artificial Photosynthesis at Efficiencies Greatly Exceeding That of Natural Photosynthesis. *Acc. Chem. Res.* **2019**, *52*, 3143−3148.
(24) Schilter, D.; Camara, J. M.; Huynh, M. T.; Hammes-Schiffer, S.; Rauchfuss, T. B. Hydrogenase Enzymes and Their Synthetic Models: The Role of Metal Hydrides. *Chem. Rev.* **2016**, *116*, 8693−8749.
(25) Lubitz, W.; Ogata, H.; Rüdiger, O.; Reijerse, E. Hydrogenases. *Chem. Rev.* **2014**, *114*, 4081−4148.
(26) Peters, J. W.; Schut, G. J.; Boyd, E. S.; Mulder, D. W.; Shepard, E. M.; Broderick, J. B.; King, P. W.; Adams, M. W. W. [FeFe]- and [NiFe]-Hydrogenase Diversity, Mechanism, and Maturation. *Biochim. Biophys. Acta, Mol. Cell Res.* **2015**, *1853*, 1350−1369.
(27) Corr, M. J.; Murphy, J. A. Evolution in the Understanding of [Fe]-Hydrogenase. *Chem. Soc. Rev.* **2011**, *40*, 2279−2292.
(28) Pershad, H. R.; Duff, J. L. C.; Heering, H. A.; Duin, E. C.; Albracht, S. P. J.; Armstrong, F. A. Catalytic Electron Transport in *Chromatium Vinosum* [NiFe]-Hydrogenase: Application of Voltammetry in Detecting Redox-Active Centers and Establishing That Hydrogen Oxidation Is Very Fast Even at Potentials Close to the Reversible H^+/H_2 Value. *Biochemistry* **1999**, *38*, 8992−8999.
(29) Madden, C.; Vaughn, M. D.; Díez-Pérez, I.; Brown, K. A.; King, P. W.; Gust, D.; Moore, A. L.; Moore, T. A. Catalytic Turnover of [FeFe]-Hydrogenase Based on Single-Molecule Imaging. *J. Am. Chem. Soc.* **2012**, *134*, 1577−1582.
(30) Hexter, S. V.; Grey, F.; Happe, T.; Climent, V.; Armstrong, F. A. Electrocatalytic Mechanism of Reversible Hydrogen Cycling by Enzymes and Distinctions between the Major Classes of Hydrogenases. *Proc. Natl. Acad. Sci. U. S. A.* **2012**, *109*, 11516−11521.
(31) George, S. J.; Kurkin, S.; Thorneley, R. N. F.; Albracht, S. P. J. Reactions of H_2, CO, and O_2 with Active [NiFe]-Hydrogenase from *Allochromatium Vinosum*. A Stopped-Flow Infrared Study. *Biochemistry* **2004**, *43*, 6808−6819.
(32) Krämer, T.; Kampa, M.; Lubitz, W.; van Gastel, M.; Neese, F. Theoretical Spectroscopy of the NiII Intermediate States in the Catalytic Cycle and the Activation of [NiFe] Hydrogenases. *ChemBioChem* **2013**, *14*, 1898−1905.
(33) Roberts, L. M.; Lindahl, P. A. Stoichiometric Reductive Titrations of *Desulfovibrio Gigas* Hydrogenase. *J. Am. Chem. Soc.* **1995**, *117*, 2565−2572.
(34) Whitehead, J. P.; Gurbiel, R. J.; Bagyinka, C.; Hoffman, B. M.; Maroney, M. J. The Hydrogen Binding Site in Hydrogenase: 35-GHz ENDOR and XAS Studies of the Nickel-C (Reduced and Active Form) and the Ni-L Photoproduct. *J. Am. Chem. Soc.* **1993**, *115*, 5629−5635.
(35) Foerster, S.; van Gastel, M.; Brecht, M.; Lubitz, W. An Orientation-Selected ENDOR and HYSCORE Study of the Ni-C Active State of *Desulfovibrio Vulgaris* Miyazaki F Hydrogenase. *JBIC, J. Biol. Inorg. Chem.* **2005**, *10*, 51−62.
(36) De Lacey, A. L.; Fernández, V. M.; Rousset, M.; Cammack, R. Activation and Inactivation of Hydrogenase Function and the Catalytic Cycle: Spectroelectrochemical Studies. *Chem. Rev.* **2007**, *107*, 4304−4330.
(37) Ogata, H.; Nishikawa, K.; Lubitz, W. Hydrogens Detected by Subatomic Resolution Protein Crystallography in a [NiFe] Hydrogenase. *Nature* **2015**, *520*, 571−574.
(38) Tai, H.; Nishikawa, K.; Higuchi, Y.; Mao, Z.; Hirota, S. Cysteine SH and Glutamate COOH Contributions to [NiFe] Hydrogenase Proton Transfer Revealed by Highly Sensitive FTIR Spectroscopy. *Angew. Chem.* **2019**, *131*, 13419−13424.
(39) van der Zwaan, J. W.; Albracht, S. P. J.; Fontijn, R. D.; Slater, E. C. Monovalent Nickel in Hydrogenase from *Chromatium Vinosum*. *FEBS Lett.* **1985**, *179*, 271−277.
(40) Bagley, K. A.; Duin, E. C.; Roseboom, W.; Albracht, S. P. J.; Woodruff, W. H. Infrared-Detectable Group Senses Changes in Charge Density on the Nickel Center in Hydrogenase from Chromatium Vinosum. *Biochemistry* **1995**, *34* (16), 5527−5535.
(41) Spek, T. M. V. D.; Arendsen, A. F.; Happe, R. P.; Yun, S.; Bagley, K. A.; Stufkens, D. J.; Hagen, W. R.; Albracht, S. P. J. Similarities in the Architecture of the Active Sites of Ni-Hydrogenases and Fe-

https://doi.org/10.1021/acscatal.1c04525
ACS Catal. 2021, 11, 14635−14650

Hydrogenases Detected by Means of Infrared Spectroscopy. *Eur. J. Biochem.* **1996**, *237*, 629−634.
(42) Bryant, F. O.; Adams, M. W. Characterization of Hydrogenase from the Hyperthermophilic Archaebacterium, *Pyrococcus Furiosus*. *J. Biol. Chem.* **1989**, *264*, 5070−5079.
(43) Greene, B. L.; Wu, C.-H.; McTernan, P. M.; Adams, M. W. W.; Dyer, R. B. Proton-Coupled Electron Transfer Dynamics in the Catalytic Mechanism of a [NiFe]-Hydrogenase. *J. Am. Chem. Soc.* **2015**, *137*, 4558−4566.
(44) Greene, B. L.; Wu, C.-H.; Vansuch, G. E.; Adams, M. W. W.; Dyer, R. B. Proton Inventory and Dynamics in the Ni_a-S to Ni_a-C Transition of a [NiFe] Hydrogenase. *Biochemistry* **2016**, *55*, 1813−1825.
(45) Czochralska, B.; Lindqvist, L. Diphotonic One-Electron Oxidation of NADH on Laser Excitation at 353 nm. *Chem. Phys. Lett.* **1983**, *101*, 297−299.
(46) Greene, B. L.; Vansuch, G. E.; Wu, C.-H.; Adams, M. W. W.; Dyer, R. B. Glutamate Gated Proton-Coupled Electron Transfer Activity of a [NiFe]-Hydrogenase. *J. Am. Chem. Soc.* **2016**, *138*, 13013−13021.
(47) Greene, B. L.; Vansuch, G. E.; Chica, B. C.; Adams, M. W. W.; Dyer, R. B. Applications of Photogating and Time Resolved Spectroscopy to Mechanistic Studies of Hydrogenases. *Acc. Chem. Res.* **2017**, *50*, 2718−2726.
(48) Tai, H.; Nishikawa, K.; Suzuki, M.; Higuchi, Y.; Hirota, S. Control of the Transition between Ni-C and Ni-SIa States by the Redox State of the Proximal Fe-S Cluster in the Catalytic Cycle of [NiFe] Hydrogenase. *Angew. Chem.* **2014**, *126*, 14037−14040.
(49) Murphy, B. J.; Hidalgo, R.; Roessler, M. M.; Evans, R. M.; Ash, P. A.; Myers, W. K.; Vincent, K. A.; Armstrong, F. A. Discovery of Dark pH-Dependent H^+ Migration in a [NiFe]-Hydrogenase and Its Mechanistic Relevance: Mobilizing the Hydrido Ligand of the Ni-C Intermediate. *J. Am. Chem. Soc.* **2015**, *137*, 8484−8489.
(50) Bertrand, P.; Dole, F.; Asso, M.; Guigliarelli, B. Is There a Rate-Limiting Step in the Catalytic Cycle of [Ni-Fe] Hydrogenases? *JBIC, J. Biol. Inorg. Chem.* **2000**, *5*, 682−691.
(51) Zorin, N. A.; Dimon, B.; Gagnon, J.; Gaillard, J.; Carrier, P.; Vignais, P. M. Inhibition by Iodoacetamide and Acetylene of the H-D-Exchange Reaction Catalyzed by *Thiocapsa Roseopersicina* Hydrogenase. *Eur. J. Biochem.* **1996**, *241*, 675−681.
(52) McTavish, H.; Sayavedra-Soto, L. A.; Arp, D. J. Comparison of Isotope Exchange, H_2 Evolution, and H_2 Oxidation Activities of *Azotobacter Vinelandii* Hydrogenase. *Biochim. Biophys. Acta, Protein Struct. Mol. Enzymol.* **1996**, *1294*, 183−190.
(53) Siegbahn, P. E. M.; Liao, R.-Z. The Energetics of Hydrogen Molecule Oxidation in NiFe-Hydrogenase. *ACS Catal.* **2020**, *10*, 5603−5613.
(54) Lill, S. O. N.; Siegbahn, P. E. M. An Autocatalytic Mechanism for NiFe-Hydrogenase: Reduction to Ni(I) Followed by Oxidative Addition. *Biochemistry* **2009**, *48*, 1056−1066.
(55) Sanchez, M. L. K.; Wu, C.-H.; Adams, M. W. W.; Dyer, R. B. Optimizing Electron Transfer from CdSe QDs to Hydrogenase for Photocatalytic H_2 Production. *Chem. Commun.* **2019**, *55*, 5579−5582.
(56) Chica, B.; Wu, C.-H.; Liu, Y.; Adams, M. W. W.; Lian, T.; Dyer, R. B. Balancing Electron Transfer Rate and Driving Force for Efficient Photocatalytic Hydrogen Production in CdSe/CdS Nanorod−[NiFe] Hydrogenase Assemblies. *Energy Environ. Sci.* **2017**, *10*, 2245−2255.
(57) Sanchez, M. L. K.; Sommer, C.; Reijerse, E.; Birrell, J. A.; Lubitz, W.; Dyer, R. B. Investigating the Kinetic Competency of CrHydA1 [FeFe] Hydrogenase Intermediate States via Time-Resolved Infrared Spectroscopy. *J. Am. Chem. Soc.* **2019**, *141*, 16064−16070.
(58) Land, H.; Senger, M.; Berggren, G.; Stripp, S. T. Current State of [FeFe]-Hydrogenase Research: Biodiversity and Spectroscopic Investigations. *ACS Catal.* **2020**, *10*, 7069−7086.
(59) Ratzloff, M. W.; Artz, J. H.; Mulder, D. W.; Collins, R. T.; Furtak, T. E.; King, P. W. CO-Bridged H-Cluster Intermediates in the Catalytic Mechanism of [FeFe]-Hydrogenase CaI. *J. Am. Chem. Soc.* **2018**, *140*, 7623−7628.
(60) Birrell, J. A.; Pelmenschikov, V.; Mishra, N.; Wang, H.; Yoda, Y.; Tamasaku, K.; Rauchfuss, T. B.; Cramer, S. P.; Lubitz, W.; DeBeer, S. Spectroscopic and Computational Evidence That [FeFe] Hydrogenases Operate Exclusively with CO-Bridged Intermediates. *J. Am. Chem. Soc.* **2020**, *142*, 222−232.
(61) Silakov, A.; Kamp, C.; Reijerse, E.; Happe, T.; Lubitz, W. Spectroelectrochemical Characterization of the Active Site of the [FeFe] Hydrogenase HydA1 from *Chlamydomonas Reinhardtii*. *Biochemistry* **2009**, *48*, 7780−7786.
(62) Schut, G. J.; Adams, M. W. W. The Iron-Hydrogenase of *Thermotoga Maritima* Utilizes Ferredoxin and NADH Synergistically: A New Perspective on Anaerobic Hydrogen Production. *J. Bacteriol.* **2009**, *191*, 4451−4457.
(63) Greene, B. L.; Schut, G. J.; Adams, M. W. W.; Dyer, R. B. Pre-Steady-State Kinetics of Catalytic Intermediates of an [FeFe]-Hydrogenase. *ACS Catal.* **2017**, *7*, 2145−2150.
(64) Chongdar, N.; Pawlak, K.; Rüdiger, O.; Reijerse, E. J.; Rodríguez-Maciá, P.; Lubitz, W.; Birrell, J. A.; Ogata, H. Spectroscopic and Biochemical Insight into an Electron-Bifurcating [FeFe] Hydrogenase. *JBIC, J. Biol. Inorg. Chem.* **2020**, *25*, 135−149.
(65) Happe, T.; Naber, J. D. Isolation, Characterization and N-Terminal Amino Acid Sequence of Hydrogenase from the Green Alga *Chlamydomonas Reinhardtii*. *Eur. J. Biochem.* **1993**, *214*, 475−481.
(66) Mulder, D. W.; Boyd, E. S.; Sarma, R.; Lange, R. K.; Endrizzi, J. A.; Broderick, J. B.; Peters, J. W. Stepwise [FeFe]-Hydrogenase H-Cluster Assembly Revealed in the Structure of HydA ΔEFG. *Nature* **2010**, *465*, 248−251.
(67) Berggren, G.; Adamska, A.; Lambertz, C.; Simmons, T. R.; Esselborn, J.; Atta, M.; Gambarelli, S.; Mouesca, J.-M.; Reijerse, E.; Lubitz, W.; Happe, T.; Artero, V.; Fontecave, M. Biomimetic Assembly and Activation of [FeFe]-Hydrogenases. *Nature* **2013**, *499*, 66−69.
(68) Siebel, J. F.; Adamska-Venkatesh, A.; Weber, K.; Rumpel, S.; Reijerse, E.; Lubitz, W. Hybrid [FeFe]-Hydrogenases with Modified Active Sites Show Remarkable Residual Enzymatic Activity. *Biochemistry* **2015**, *54*, 1474−1483.
(69) Liu, J.; Chakraborty, S.; Hosseinzadeh, P.; Yu, Y.; Tian, S.; Petrik, I.; Bhagi, A.; Lu, Y. Metalloproteins Containing Cytochrome, Iron−Sulfur, or Copper Redox Centers. *Chem. Rev.* **2014**, *114*, 4366−4469.
(70) Lockwood, C. W. J.; Burlat, B.; Cheesman, M. R.; Kern, M.; Simon, J.; Clarke, T. A.; Richardson, D. J.; Butt, J. N. Resolution of Key Roles for the Distal Pocket Histidine in Cytochrome c Nitrite Reductases. *J. Am. Chem. Soc.* **2015**, *137*, 3059−3068.
(71) Geier, B. M.; Schägger, H.; Ortwein, C.; Link, T. A.; Hagen, W. R.; Brandt, U.; Jagow, G. V. Kinetic Properties and Ligand Binding of the Eleven-Subunit Cytochrome-c Oxidase from *Saccharomyces Cerevisiae* Isolated with a Novel Large-Scale Purification Method. *Eur. J. Biochem.* **1995**, *227*, 296−302.
(72) Pines, E.; Huppert, D. PH Jump: A Relaxational Approach. *J. Phys. Chem.* **1983**, *87*, 4471−4478.
(73) Rosell, F. I.; Mauk, A. G. Photochemical Reagents for the Study of Metalloproteins by Flash Photolysis. *Coord. Chem. Rev.* **2011**, *255*, 737−756.
(74) McCray, J. A.; Herbette, L.; Kihara, T.; Trentham, D. R. A New Approach to Time-Resolved Studies of ATP-Requiring Biological Systems; Laser Flash Photolysis of Caged ATP. *Proc. Natl. Acad. Sci. U. S. A.* **1980**, *77*, 7237−7241.
(75) Seefeldt, L. C.; Hoffman, B. M.; Peters, J. W.; Raugei, S.; Beratan, D. N.; Antony, E.; Dean, D. R. Energy Transduction in Nitrogenase. *Acc. Chem. Res.* **2018**, *51*, 2179−2186.
(76) Fuchs, G.; Boll, M.; Heider, J. Microbial degradation of aromatic compounds − from one strategy to four. *Nat. Rev. Microbiol.* **2011**, *9*, 803−816.
(77) Yang, Z.-Y.; Ledbetter, R.; Shaw, S.; Pence, N.; Tokmina-Lukaszewska, M.; Eilers, B.; Guo, Q.; Pokhrel, N.; Cash, V. L.; Dean, D. R.; Antony, E.; Bothner, B.; Peters, J. W.; Seefeldt, L. C. Evidence That the P_i Release Event Is the Rate-Limiting Step in the Nitrogenase Catalytic Cycle. *Biochemistry* **2016**, *55*, 3625−3635.

https://doi.org/10.1021/acscatal.1c04525
ACS Catal. 2021, 11, 14635−14650

(78) Edwards, E. H.; Bren, K. L. Light-Driven Catalysis with Engineered Enzymes and Biomimetic Systems. *Biotechnol. Appl. Biochem.* **2020**, *67*, 463−483.
(79) Zheng, D.; Zhang, Y.; Liu, X.; Wang, J. Coupling Natural Systems with Synthetic Chemistry for Light-Driven Enzymatic Biocatalysis. *Photosynth. Res.* **2020**, *143*, 221−231.
(80) Kornienko, N.; Zhang, J. Z.; Sakimoto, K. K.; Yang, P.; Reisner, E. Interfacing Nature's Catalytic Machinery with Synthetic Materials for Semi-Artificial Photosynthesis. *Nat. Nanotechnol.* **2018**, *13*, 890−899.
(81) Nocera, D. G.; Winkler, J. R.; Yocom, K. M.; Bordignon, E.; Gray, H. B. Kinetics of Intermolecular and Intramolecular Electron Transfer from Ruthenium(II) Complexes to Ferricytochrome c. *J. Am. Chem. Soc.* **1984**, *106*, 5145−5150.
(82) Pizano, A. A.; Lutterman, D. A.; Holder, P. G.; Teets, T. S.; Stubbe, J.; Nocera, D. G. Photo-Ribonucleotide Reductase B2 by Selective Cysteine Labeling with a Radical Phototrigger. *Proc. Natl. Acad. Sci. U. S. A.* **2012**, *109*, 39−43.
(83) Zadvornyy, O. A.; Lucon, J. E.; Gerlach, R.; Zorin, N. A.; Douglas, T.; Elgren, T. E.; Peters, J. W. Photo-Induced H2 Production by [NiFe]-Hydrogenase from *T. Roseopersicina* Covalently Linked to a Ru(II) Photosensitizer. *J. Inorg. Biochem.* **2012**, *106*, 151−155.
(84) Tran, N.-H.; Huynh, N.; Bui, T.; Nguyen, Y.; Huynh, P.; Cooper, M. E.; Cheruzel, L. E. Light-Initiated Hydroxylation of Lauric Acid Using Hybrid P450 BM3 Enzymes. *Chem. Commun.* **2011**, *47*, 11936−11938.
(85) Lubner, C. E.; Applegate, A. M.; Knörzer, P.; Ganago, A.; Bryant, D. A.; Happe, T.; Golbeck, J. H. Solar Hydrogen-Producing Bionanodevice Outperforms Natural Photosynthesis. *Proc. Natl. Acad. Sci. U. S. A.* **2011**, *108*, 20988−20991.
(86) Reisner, E.; Powell, D. J.; Cavazza, C.; Fontecilla-Camps, J. C.; Armstrong, F. A. Visible Light-Driven H_2 Production by Hydrogenases Attached to Dye-Sensitized TiO_2 Nanoparticles. *J. Am. Chem. Soc.* **2009**, *131*, 18457−18466.
(87) Greene, B. L.; Joseph, C. A.; Maroney, M. J.; Dyer, R. B. Direct Evidence of Active-Site Reduction and Photodriven Catalysis in Sensitized Hydrogenase Assemblies. *J. Am. Chem. Soc.* **2012**, *134*, 11108−11111.
(88) Brown, K. A.; Dayal, S.; Ai, X.; Rumbles, G.; King, P. W. Controlled Assembly of Hydrogenase-CdTe Nanocrystal Hybrids for Solar Hydrogen Production. *J. Am. Chem. Soc.* **2010**, *132*, 9672−9680.
(89) Caputo, C. A.; Gross, M. A.; Lau, V. W.; Cavazza, C.; Lotsch, B. V.; Reisner, E. Photocatalytic Hydrogen Production Using Polymeric Carbon Nitride with a Hydrogenase and a Bioinspired Synthetic Ni Catalyst. *Angew. Chem., Int. Ed.* **2014**, *53*, 11538−11542.
(90) Miller, M.; Robinson, W. E.; Oliveira, A. R.; Heidary, N.; Kornienko, N.; Warnan, J.; Pereira, I. A. C.; Reisner, E. Interfacing Formate Dehydrogenase with Metal Oxides for the Reversible Electrocatalysis and Solar-Driven Reduction of Carbon Dioxide. *Angew. Chem., Int. Ed.* **2019**, *58*, 4601−4605.
(91) Woolerton, T. W.; Sheard, S.; Reisner, E.; Pierce, E.; Ragsdale, S. W.; Armstrong, F. A. Efficient and Clean Photoreduction of CO_2 to CO by Enzyme-Modified TiO_2 Nanoparticles Using Visible Light. *J. Am. Chem. Soc.* **2010**, *132*, 2132−2133.
(92) Brown, K. A.; Harris, D. F.; Wilker, M. B.; Rasmussen, A.; Khadka, N.; Hamby, H.; Keable, S.; Dukovic, G.; Peters, J. W.; Seefeldt, L. C.; King, P. W. Light-Driven Dinitrogen Reduction Catalyzed by a CdS:Nitrogenase MoFe Protein Biohybrid. *Science* **2016**, *352*, 448−450.
(93) Lee, S. H.; Choi, D. S.; Kuk, S. K.; Park, C. B. Photobiocatalysis: Activating Redox Enzymes by Direct or Indirect Transfer of Photoinduced Electrons. *Angew. Chem., Int. Ed.* **2018**, *57*, 7958−7985.
(94) Chica, B.; Ruzicka, J.; Kallas, H.; Mulder, D. W.; Brown, K. A.; Peters, J. W.; Seefeldt, L. C.; Dukovic, G.; King, P. W. Defining Intermediates of Nitrogenase MoFe Protein during N_2 Reduction under Photochemical Electron Delivery from CdS Quantum Dots. *J. Am. Chem. Soc.* **2020**, *142*, 14324−14330.
(95) Reichard, P. From RNA to DNA, Why so Many Ribonucleotide Reductases? *Science* **1993**, *260*, 1773−1777.
(96) Kang, G.; Taguchi, A. T.; Stubbe, J.; Drennan, C. L. Structure of a Trapped Radical Transfer Pathway within a Ribonucleotide Reductase Holocomplex. *Science* **2020**, *368*, 424−427.
(97) Minnihan, E. C.; Nocera, D. G.; Stubbe, J. Reversible, Long-Range Radical Transfer in *E. Coli* Class Ia Ribonucleotide Reductase. *Acc. Chem. Res.* **2013**, *46*, 2524−2535.
(98) Ge, J.; Yu, G.; Ator, M. A.; Stubbe, J. Pre-Steady-State and Steady-State Kinetic Analysis of *E. Coli* Class I Ribonucleotide Reductase. *Biochemistry* **2003**, *42*, 10071−10083.
(99) Greene, B. L.; Stubbe, J.; Nocera, D. G. Selenocysteine Substitution in a Class I Ribonucleotide Reductase. *Biochemistry* **2019**, *58*, 5074−5084.
(100) Minnihan, E. C.; Seyedsayamdost, M. R.; Uhlin, U.; Stubbe, J. Kinetics of Radical Intermediate Formation and Deoxynucleotide Production in 3-Aminotyrosine-Substituted *Escherichia Coli* Ribonucleotide Reductases. *J. Am. Chem. Soc.* **2011**, *133*, 9430−9440.
(101) Minnihan, E. C.; Seyedsayamdost, M. R.; Stubbe, J. Use of 3-Aminotyrosine To Examine the Pathway Dependence of Radical Propagation in *Escherichia Coli* Ribonucleotide Reductase. *Biochemistry* **2009**, *48*, 12125−12132.
(102) Chang, M. C. Y.; Yee, C. S.; Stubbe, J.; Nocera, D. G. Turning on Ribonucleotide Reductase by Light-Initiated Amino Acid Radical Generation. *Proc. Natl. Acad. Sci. U. S. A.* **2004**, *101*, 6882−6887.
(103) Reece, S. Y.; Seyedsayamdost, M. R.; Stubbe, J.; Nocera, D. G. Direct Observation of a Transient Tyrosine Radical Competent for Initiating Turnover in a Photochemical Ribonucleotide Reductase. *J. Am. Chem. Soc.* **2007**, *129*, 13828−13830.
(104) Reece, S. Y.; Seyedsayamdost, M. R.; Stubbe, J.; Nocera, D. G. Photoactive Peptides for Light-Initiated Tyrosyl Radical Generation and Transport into Ribonucleotide Reductase. *J. Am. Chem. Soc.* **2007**, *129*, 8500−8509.
(105) Pizano, A. A.; Olshansky, L.; Holder, P. G.; Stubbe, J.; Nocera, D. G. Modulation of Y356 Photooxidation in E. Coli Class Ia Ribonucleotide Reductase by Y731 Across the $\alpha 2{:}\beta 2$ Interface. *J. Am. Chem. Soc.* **2013**, *135*, 13250−13253.
(106) Olshansky, L.; Stubbe, J.; Nocera, D. G. Charge-Transfer Dynamics at the α/β Subunit Interface of a Photochemical Ribonucleotide Reductase. *J. Am. Chem. Soc.* **2016**, *138*, 1196−1205.
(107) Ravichandran, K. R.; Taguchi, A. T.; Wei, Y.; Tommos, C.; Nocera, D. G.; Stubbe, J. A > 200 MeV Uphill Thermodynamic Landscape for Radical Transport in Escherichia Coli Ribonucleotide Reductase Determined Using Fluorotyrosine-Substituted Enzymes. *J. Am. Chem. Soc.* **2016**, *138*, 13706−13716.
(108) Seyedsayamdost, M. R.; Reece, S. Y.; Nocera, D. G.; Stubbe, J. Mono-, Di-, Tri-, and Tetra-Substituted Fluorotyrosines: New Probes for Enzymes That Use Tyrosyl Radicals in Catalysis. *J. Am. Chem. Soc.* **2006**, *128*, 1569−1579.
(109) Ravichandran, K. R.; Zong, A. B.; Taguchi, A. T.; Nocera, D. G.; Stubbe, J.; Tommos, C. Formal Reduction Potentials of Difluorotyrosine and Trifluorotyrosine Protein Residues: Defining the Thermodynamics of Multistep Radical Transfer. *J. Am. Chem. Soc.* **2017**, *139*, 2994−3004.
(110) Olshansky, L.; Pizano, A. A.; Wei, Y.; Stubbe, J.; Nocera, D. G. Kinetics of Hydrogen Atom Abstraction from Substrate by an Active Site Thiyl Radical in Ribonucleotide Reductase. *J. Am. Chem. Soc.* **2014**, *136*, 16210−16216.
(111) Lee, W.; Kasanmascheff, M.; Huynh, M.; Quartararo, A.; Costentin, C.; Bejenke, I.; Nocera, D. G.; Bennati, M.; Tommos, C.; Stubbe, J. Properties of Site-Specifically Incorporated 3-Aminotyrosine in Proteins To Study Redox-Active Tyrosines: *Escherichia Coli* Ribonucleotide Reductase as a Paradigm. *Biochemistry* **2018**, *57*, 3402−3415.
(112) Kasanmascheff, M.; Lee, W.; Nick, T. U.; Stubbe, J.; Bennati, M. Radical Transfer in E. Coli Ribonucleotide Reductase: A NH2Y731/R411A-α Mutant Unmasks a New Conformation of the Pathway Residue 731. *Chem. Sci.* **2016**, *7*, 2170−2178.
(113) Greene, B. L.; Taguchi, A. T.; Stubbe, J.; Nocera, D. G. Conformationally Dynamic Radical Transfer within Ribonucleotide Reductase. *J. Am. Chem. Soc.* **2017**, *139*, 16657−16665.

https://doi.org/10.1021/acscatal.1c04525
ACS Catal. 2021, 11, 14635−14650

(114) Lin, Q.; Parker, M. J.; Taguchi, A. T.; Ravichandran, K.; Kim, A.; Kang, G.; Shao, J.; Drennan, C. L.; Stubbe, J. Glutamate 52-β at the α/β Subunit Interface of *Escherichia Coli* Class Ia Ribonucleotide Reductase Is Essential for Conformational Gating of Radical Transfer. *J. Biol. Chem.* **2017**, *292*, 9229−9239.
(115) Lundin, D.; Torrents, E.; Poole, A. M.; Sjöberg, B.-M. RNRdb, a Curated Database of the Universal Enzyme Family Ribonucleotide Reductase, Reveals a High Level of Misannotation in Sequences Deposited to Genbank. *BMC Genomics* **2009**, *10*, 589.
(116) Greene, B. L.; Stubbe, J.; Nocera, D. G. Photochemical Rescue of a Conformationally Inactivated Ribonucleotide Reductase. *J. Am. Chem. Soc.* **2018**, *140*, 15744−15752.
(117) Cui, C.; Greene, B. L.; Kang, G.; Drennan, C. L.; Stubbe, J.; Nocera, D. G. Gated Proton Release during Radical Transfer at the Subunit Interface of Ribonucleotide Reductase. *J. Am. Chem. Soc.* **2021**, *143*, 176−183.
(118) Reinhardt, C. R.; Li, P.; Kang, G.; Stubbe, J.; Drennan, C. L.; Hammes-Schiffer, S. Conformational Motions and Water Networks at the α/β Interface in *E. Coli* Ribonucleotide Reductase. *J. Am. Chem. Soc.* **2020**, *142*, 13768−13778.
(119) Olshansky, L.; Greene, B. L.; Finkbeiner, C.; Stubbe, J.; Nocera, D. G. Photochemical Generation of a Tryptophan Radical within the Subunit Interface of Ribonucleotide Reductase. *Biochemistry* **2016**, *55*, 3234−3240.

https://doi.org/10.1021/acscatal.1c04525
ACS Catal. 2021, 11, 14635−14650